energies

MDPI

Article

Prediction of Global Solar Irradiance on Parallel Rows of Tilted Surfaces Including the Effect of Direct and Anisotropic Diffuse Shading

Sara Pereira [1,*], Paulo Canhoto [1,2] and Rui Salgado [1,3]

[1] Institute of Earth Sciences, University of Évora, Rua Romão Ramalho 59, 7000-671 Évora, Portugal
[2] Department of Mechatronics Engineering, University of Évora, Rua Romão Ramalho 59, 7000-671 Évora, Portugal
[3] Physics Department, University of Évora, Rua Romão Ramalho 59, 7000-671 Évora, Portugal
* Correspondence: spereira@uevora.pt

Abstract: Solar photovoltaic power plants typically consist of rows of solar panels, where the accurate estimation of solar irradiance on inclined surfaces significantly impacts energy generation. Existing practices often only account for the first row, neglecting shading from subsequent rows. In this work, ten transposition models were assessed against experimental data and a transposition model for inner rows was developed and validated. The developed model incorporates view factors and direct and circumsolar irradiances shading from adjacent rows, significantly improving global tilted irradiance (GTI) estimates. This model was validated against one-minute observations recorded between 14 April and 1 June 2022, at Évora, Portugal (38.5306, −8.0112) resulting in values of mean bias error (MBE) and root-mean-squared error (RMSE) of −12.9 W/m^2 and 76.8 W/m^2, respectively, which represent an improvement of 368.3 W/m^2 in the MBE of GTI estimations compared to the best-performing transposition model for the first row. The proposed model was also evaluated in an operational forecast setting where corrected forecasts of direct and diffuse irradiance (0 to 72 h ahead) were used as inputs, resulting in an MBE and RMSE of −33.6 W/m^2 and 169.7 W/m^2, respectively. These findings underscore the potential of the developed model to enhance solar energy forecasting accuracy and operational algorithms' efficiency and robustness.

Keywords: solar radiation; solar energy; transposition model; solar power plant; forecast

Citation: Pereira, S.; Canhoto, P.; Salgado, R. Prediction of Global Solar Irradiance on Parallel Rows of Tilted Surfaces Including the Effect of Direct and Anisotropic Diffuse Shading. *Energies* **2024**, *17*, 3444. https://doi.org/10.3390/en17143444

Academic Editors: Annamaria Buonomano, Jayanta Deb Mondol and Biplab Das

Received: 6 June 2024
Revised: 5 July 2024
Accepted: 10 July 2024
Published: 12 July 2024

1. Introduction

In recent decades, there has been a significant surge in the installed capacity of PV systems. In 2022 alone, solar photovoltaics comprised two-thirds of the new renewable energy capacity added to the grid, totaling 239 GW [1]. This growth is driven by global efforts to decarbonize the economy and achieve net-zero greenhouse gas emissions by 2050. The International Energy Agency (IEA) estimates that PV systems will continue to expand, with new capacity projected to exceed 700 GW by 2028 [2]. With the rapid increase in the installed capacity of solar energy systems worldwide and the characteristic variability of solar radiation, accurate estimation and forecasting of power output is becoming increasingly important. The factor that most affects this output is the irradiance incident on the solar energy collectors. However, weather stations, satellites, and numerical weather prediction (NWP) models usually provide global (GHI) and diffuse (DIF) irradiance data on the horizontal plane and direct irradiance on a plane normal to the sun's rays (DNI). Therefore, transposition models that can compute the irradiance incident on a tilted surface from the available variables are essential.

Various transposition models have been developed and studied over the years. They can be divided into analytical, semi-empirical, and empirical models [3]. Analytical models are

based on the laws of physics and only require the geometric characteristics and position data of the surface, while semi-empirical and empirical models also rely on observation data.

Physical models are usually based on the sum of the direct, diffuse, and reflected irradiances on the tilted surface. The computation of the direct and reflected components is often the same for all models, with the computation of the diffuse irradiance being the distinct factor [4]. Among these models, some assume a uniform sky dome radiance with the same intensity in all directions, termed isotropic. Anisotropic models, on the other hand, define indices representing the irradiance intensity from different regions of the sky dome, such as the circumsolar region (an annular region surrounding the sun disk), the horizon-brightening region (a band along the horizon), and the background or remaining region often called the isotropic region.

Transposition models also tend to show varying degrees of performance depending on sky conditions, whether clear, cloudy, or overcast [5]. The complexity and variability of the shape and position of clouds make the accurate instantaneous evaluation of the diffuse component extremely difficult without knowing the distribution of sky radiance. A model considering this would be more complex and require not only the simple measurement of the irradiance on the tilted plane but many more variables that are not commonly measured, such as the spectral radiance. Thus, physical models must rely on assumptions that can result in high transient errors [6]. Some of the most referenced analytical physical models in the literature are reviewed in this work, such as the Klucher [7], Hay–Davies [8], and Modified Bugler [9] models. On the other hand, abundant research on the comparison of the different models at different locations and positions of the surfaces has been published [3,4,10,11]. From these, no single model emerges as the best for all studied locations/positions, but it has been widely demonstrated that anisotropic models tend to outperform isotropic models when compared to measured data because they consider the angular dependence of sky radiance, thus reflecting real-world conditions more closely compared to isotropic models.

Semi-empirical and empirical models, including machine learning approaches which are data-driven, tend to be site-dependent, which means that they are biased towards specific locations and/or tilt and azimuth angles [12–16], and will not be considered here. While these models are gaining relevance and can provide substantial benefits in some situations, their applicability is often limited because extensive local experimental data are required for the model calibration. This increases the challenge and difficulty of generalizing them to different geographic locations or environmental conditions. Given the focus of this study on developing a transposition model that is applicable across various conditions without the need for site-specific parameter adjustments, these models were excluded to maintain a broader applicability and robustness of proposed approach.

Most transposition models have been developed for a tilted surface in an open field. However, a solar energy power plant, such as photovoltaic power plants, comprises several rows of modules, where rows other than the first have a different view of the sky dome and the ground compared to the first row. Therefore, when computing the global tilted irradiance (GTI) on a panel not located in the front row, the transposition model should be adjusted to account for the fraction of the sky dome obscured by the rows at the front, as well as the possible blocking of the direct beam and circumsolar irradiance from the sun disk and the reflected irradiance coming from the front row and the ground between them. Since in large solar power plants the number of panels in the first row can be much smaller than the number of panels in the remaining rows, having a more accurate transposition model for these panels can improve the estimation of power output. Few authors have focused on this aspect, with the most notable and recent works being those by Applebaum et al. [17], Varga and Mayer [18], and Tschopp et al. [19].

As mentioned above, one aspect of higher complexity in transposition models is the parametrization of diffuse irradiance. This component of the GTI is strongly related to the diffuse horizontal irradiance (DIF) and the global horizontal irradiance (GHI), which are typically measured in radiometric stations. However, if only GHI is measured, a

separation method is needed to estimate DNI and DIF. If there are no measurements at the location of interest, estimations or forecast values need to be used instead. This increases the uncertainty associated with the estimation of GTI and, consequently, of power output. Of particular interest in this work is the usage of forecast values of solar radiation components, with the goal of predicting power output in a time horizon up to three days with an acceptable accuracy. In this regard, when utilizing forecast DNI and DIF as inputs, a transposition model allows for the forecasting of GTI and power output of photovoltaic systems if coupled with thermal and electric models of photovoltaic systems.

These forecasts can be obtained from a global operational numerical weather prediction model (NWP) such as the Integrated Forecasting System (IFS) of the European Centre for Medium-range Forecasts (ECMWF) [20]. By incorporating constitutive and state equations describing physical phenomena in the atmosphere, subject to boundary and initial conditions, NWP models provide the evolution of the atmospheric state, which include surface-level GHI. In the case of IFS/ECMWFS, DNI is also included, allowing for the study and assessment of solar resources and operational forecasts [21,22].

This work presents a comprehensive review of transposition models, categorizing models that do not include shading or irradiance masking as "first-row models", and those that include these aspects as "inner-row models". The development of a transposition model for inner rows is also presented, which can be applied to a desired first-row model. The proposed model is validated using experimental values, which are also used for the assessment and comparison of all models. The use of operational forecasts of solar irradiance is assessed to estimate the impact of the accuracy of the transposition model on GTI prediction at different time horizons. The primary aim is to develop a transposition model for inner rows of solar power plants, validate the proposed model against experimental measurements, and evaluate its performance using operational solar radiation forecasts. This study addresses gaps in the existing literature, which mainly focuses on the first row of panels, neglecting the impact of direct and anisotropic diffuse shading on inner rows. The hypotheses focus on the expected improvement in the accuracy of the developed model's results over existing models for the first row, as well as its robustness when used with forecasted irradiance data as input.

This paper is organized as follows: An initial review of the most used analytical models and recent models developed for rows that are not the first is presented in Section 2. Section 3 details the development of a transposition model based on the works of Tschopp et al. and Varga and Mayer [18,19] for surfaces not located in the first row. Section 4 presents the experimental setup and procedure for testing the different models, and Section 5 discusses the evaluation and results. Section 6 establishes a connection with solar irradiance forecasting by applying the developed model to forecasted values of direct normal and diffuse horizontal irradiance, integrating it as an essential part of an operational algorithm for forecasting solar irradiance on a tilted surface. Finally, Section 7 presents the conclusions of this work.

2. Solar Irradiance Transposition Models for Tilted Surfaces

This section provides a review of analytical transposition models, ranging from the most widely used and commonly referenced transposition models that do not consider shading and obscuration to the few and most recently proposed models designed for inner rows in solar power plants.

2.1. Transposition Models for the First Row of Collectors in Solar Power Plants

For modeling solar irradiance on a tilted surface (*GTI*), nine of the most commonly used analytical transposition models are reviewed, where one is isotropic and the remaining are anisotropic models. In all the following equations, α is the solar height, Φ is the solar zenith angle, γ_s is the solar azimuth, θ is the incidence angle on the surface, β is the tilt angle of the surface, and γ_p is the azimuth of the surface, taking the horizontal plane and the local meridian as references.

Analytical transposition models include the computation of tilt factors for determining the beam (R_b), diffuse (R_d), and reflected (R_r) irradiances on the tilted surface. These factors are used in Equation (1) for determining GTI, where DHI is the direct horizontal irradiance as defined in Equation (2):

$$GTI = R_b DHI + R_d DIF + R_r GHI \tag{1}$$

$$DHI = DNI \times \cos(\Phi) \tag{2}$$

For the first row of photovoltaic panels, assuming no obstruction of the sun's rays, the direct irradiance on the tilted plane can be calculated at any given instant by multiplying DHI with the beam radiation tilt factor described in Equation (3):

$$R_b = \frac{\cos(\theta)}{\cos(\Phi)} \tag{3}$$

The irradiance reflected onto the tilted surface by the surrounding surfaces is assumed isotropic and is modeled by multiplying GHI with the reflected irradiance tilt factor R_r (Equation (4)), which consists of the product of the albedo of the surrounding ground (ρ_g) and the view factor F_g (Equation (5)).

$$R_r = \rho_g F_g, \tag{4}$$

$$F_g = \frac{1 - \cos(\beta)}{2} \tag{5}$$

Numerous models have been proposed for determining the diffuse tilt factor R_d since the diffuse radiation is highly variable due to its dependency on atmospheric conditions. Models that consider the diffuse irradiance on a tilted surface coming from the entire sky dome to have the same intensity are isotropic, while others that divide the sky dome into regions with different intensities of diffuse radiance are called anisotropic models. These regions are usually the circumsolar region, which constitutes an annular region surrounding the sun, i.e., the horizon-brightening region, which is the region of the sky dome near the horizon, and the remaining sky dome region is termed the isotropic region.

In the following, several models are presented, including the widely used isotropic model that was developed by Liu and Jordan [23]. It assumes that the diffuse solar radiation is uniformly spread across the sky, which simplifies the calculation of solar radiation on inclined surfaces by considering the sky as a homogenous light source. This model only considers the tilt angle of the surface as input, as presented in Equations (6) and (7), where the diffuse tilt factor is simply a view factor between the surface and the sky. Its advantages lie in its simplicity and widespread adoption for preliminary solar energy designs and studies. However, the model's accuracy can be compromised due to its isotropic assumption, leading to potential inaccuracies in non-homogenous sky conditions and environments with significant obstructions. Despite these limitations, it remains a significant tool in solar energy research and engineering, often serving as a benchmark for more complex anisotropic models that account for the directional distribution of diffuse radiation.

Liu and Jordan model (LJ):

$$R_d = F_s \tag{6}$$

$$F_s = \frac{1 + \cos(\beta)}{2} \tag{7}$$

The remaining models analyzed are anisotropic models, which are often more representative of real sky conditions.

Bugler model (B):

The Bugler model [24] includes a circumsolar region in which its contribution to the diffuse irradiance is assumed to be 5% of DNI and can be computed using Equation (8), where F_s is the sky view factor given by Equation (7). Bugler derived this model by analyz-

ing solar radiation data and developing equations that incorporate these anisotropic factors, resulting in more accurate predictions of solar irradiance on tilted surfaces. However, this model overlooks the contribution of the circumsolar region to the isotropic irradiance and was later modified.

$$R_d = F_s + 0.05\frac{DHI \times R_b}{DIF} \tag{8}$$

Temps and Coulson model (TC):

The Temps and Coulson [25] model, defined by Equation (9), considers the circumsolar region through the factor $\left[1 + cos^2(\theta)sin^3(\Phi)\right]$ and the horizon brightening through $\left[1 + sin^3\left(\frac{\beta}{2}\right)\right]$. This model was obtained through measurements of direct and diffuse solar flux incident on slopes of various orientations for clear-sky conditions through a pyranometer.

$$R_d = F_s\left[1 + cos^2(\theta)sin^3(\Phi)\right]\left[1 + sin^3\left(\frac{\beta}{2}\right)\right] \tag{9}$$

Klucher model (K):

The Klucher model [7], given by Equation (10), is similar to the Temps and Coulson model, except for the inclusion of the clearness index f, defined by Equation (11). Under overcast conditions, this model reduces to the isotropic model (where f tends to 0). It was derived from a 6-month dataset of measured hourly diffuse and total solar radiation on a horizontal plane and total radiation on surfaces with 0° azimuth and tilts of 37° and 60°.

$$R_d = F_s\left[1 + fsin^3\left(\frac{\beta}{2}\right)\right]\left[1 + fcos^2(\theta)sin^3(\Phi)\right] \tag{10}$$

$$f = 1 - \left(\frac{DIF}{DHI + DIF}\right)^2 \tag{11}$$

Hay–Davies model (HD):

The Hay–Davies model [8], which does not consider horizon brightening, is given by Equation (12). Here, A is named the anisotropy index, also termed direct or beam irradiance index, and is defined in Equation (13), where ENI is the extraterrestrial normal irradiance. This index represents the total transmittance of the atmosphere for beam radiation and is used to define the portion of circumsolar ($A \times R_b$) and isotropic ($F_s(1 - A)$) diffuse irradiance on the tilted surface.

$$R_d = A \times R_b + F_s(1 - A) \tag{12}$$

$$A = \frac{DNI}{ENI} \tag{13}$$

Ma Iqbal model (MI):

The Ma Iqbal model [26], described through Equation (14), is similar to the Hay–Davies model but uses the clearness index k_T (Equation (15)) to define the circumsolar portion of diffuse irradiance instead of the direct irradiance index. The clearness index is computed as the ratio of global horizontal irradiance (GHI) to extraterrestrial horizontal irradiance (EHI). This formulation allows the Ma Iqbal model to account for varying sky conditions and solar geometry, enhancing its applicability in solar energy studies and irradiance forecasting.

$$R_d = k_T R_b + F_s(1 - k_T) \tag{14}$$

$$k_T = \frac{GHI}{EHI} \tag{15}$$

Modified Bugler model (MB):

The Modified Bugler model [9] improves the Bugler model by considering the contribution of the circumsolar region to the background isotropic diffuse radiance, computed through Equation (16). This model was validated using extensive datasets from various lo-

cations around the world. These datasets included measured solar radiation data collected under different sky conditions, such as clear sky, cloudy sky, and overcast sky conditions. Additionally, the model was validated against experimental data that accounted for various surface orientations, including horizontal, tilted, and vertical surfaces.

$$R_d = \left(1 - 0.05\frac{DHI}{DIF}\right)F_s + 0.05\frac{DHI \times R_b}{DIF} \tag{16}$$

Modified Ma Iqbal model (MMI):

The modified Ma Iqbal model (Equation (17)) [3] is similar to the original model proposed by this author but uses a clearness index (Equation (18)) adjusted with an optical air mass as defined in Equation (19) [27].

$$R_d = k\prime_T R_b + (1 - k\prime_T)F_s \text{ a} = 1, \tag{17}$$

$$k\prime_T = \frac{k_T}{1.031exp\left(\frac{-1.4}{0.9+\frac{9.4}{M}}\right) + 0.1} \tag{18}$$

$$M = \frac{1}{\cos(\Phi) + 0.15(93.885 - \Phi)^{-1.253}} \tag{19}$$

Reindl model (R):

The Reindl model [28], based on the Hay–Davies model, uses the same anisotropic index, A (Equation (13)), but includes an additional term to account for horizon brightening (Equation (20)). This model was developed based on datasets from locations across the USA.

$$R_d = A \times R_b + F_s(1 - A)\left[1 + \sqrt{\frac{DHI}{DHI + DIF}}sin^3\left(\frac{\beta}{2}\right)\right] \tag{20}$$

Perez model (P):

The Perez model, one of the most widely used transposition models in the literature, is included in this work even though it cannot be classified as an analytical model since it is built upon measured data and is subject to continuous revisions for this reason. The version of the Perez model [29] used in this work, often referred to as Perez3, is considered the most widely accepted version of this model [4]. This model categorizes the sky in three zones: the circumsolar zone, horizon band, and isotropic zone. The diffuse irradiance tilt factor is computed using Equations (21)–(27), with the assumption that the circumsolar irradiance originates from a point source and irradiance from the horizon from an infinitesimally thin region. The zenith angle is exceptionally used in radians for Equation (26). The coefficients F_{ij} were determined using data from 10 American and 3 European locations and can be consulted in [4,29].

$$R_d = F_1\frac{a}{b} + (1 - F_1)F_s + F_2\sin\beta \tag{21}$$

$$a = \max(0, \cos\theta) \tag{22}$$

$$b = \max[\cos 85^\circ, \sin(90^\circ - \theta_z)] \tag{23}$$

$$F_1 = max[0, F_{11}(\varepsilon) + F_{12}(\varepsilon)\Delta + F_{13}(\varepsilon)\theta_z] \tag{24}$$

$$F_2 = F_{21}(\varepsilon) + F_{22}(\varepsilon)\Delta + F_{23}(\varepsilon)\theta_z \tag{25}$$

$$\varepsilon = \frac{GHI/DIF + 1.041\theta_z^3}{1 + 1.041\theta_z^3} \tag{26}$$

$$\Delta = \frac{DIF}{ENI\cos\theta_z} \tag{27}$$

2.2. Transposition Models for Surfaces Not Located in the Front Row of a Solar Power Plant

The models presented in Section 2.1 were developed for a single row. In the case of photovoltaic power plants, for instance, which are composed of various parallel rows, there is a partial obscuring of the sky radiance and, eventually, the blocking of direct sun rays by the front rows over the second and subsequent rows, thus affecting the global tilted irradiance on these surfaces. An obscuring of the ground between rows can also occur, which affects the reflected irradiance.

Some authors have considered this, namely Appelbaum et al. [17], who adjusted the Klucher transposition model [7] by computing the sky view factor for the second row and adjusting the indices of the circumsolar and horizon-brightening diffuse regions. For this, the authors considered the circumsolar irradiance coming from a point source (the sun) which would be completely obscured when the obscuring angle from the sun to the base of the second row caused by the front row is higher than the sun elevation angle. The correction for the horizon-brightening region was considered near sunrise and sunset. This adjusted model was validated with data obtained in Tel Aviv, showing that for rows other than the first, the effect of the anisotropic region defined as horizon brightening is negligible.

Varga and Mayer [18] modified the Hay–Davies model [8], which does not include a horizon-brightening region, to calculate the distribution of solar irradiance along a tilted surface for rows behind the first. Besides the adjustment of the view factors, the circumsolar irradiance was corrected through the modeling of the fraction of the region obscured by the front row by considering a circumsolar region with an apparent angular radius of 15°, and the ground was divided into two sections: a shaded section that reflects only isotropic diffuse irradiance and an unshaded section that reflects global irradiance. The model was validated against power generation data from Hungary showing a clear improvement when compared to a model that only considers shading of the direct irradiance.

Tschopp et al. [19] also adjusted the Hay–Davies model for surfaces that are not on the front row by dividing the length of the surface of the row being evaluated, the back surface of the row at its front, and the ground between them in segments and then computing diffuse and direct irradiance in each segment. For this, the view factors between all segments and between each segment and the sky are computed, while the obscuring of the direct and circumsolar irradiances are determined based on a simple formula for the shadow height on the surface. The model showed a significant improvement in the estimation of GTI for rows other than the first compared to the original transposition model.

Considering this, it is expected that combining the higher detail in the modeling of shadow and circumsolar irradiance obscuration presented in [18] and the inclusion of the back surface of the row at the front and the ground between rows presented in [19] will provide better estimations of GTI for rows that are not at the front of a solar power plant.

3. Development of Transposition Model for Surfaces Not Located in the Front Row of a Solar Power Plant

The model proposed in this work for determining solar irradiance on tilted rows adjacent to the first row builds upon the models presented in [18,19].Similar to these models, it assumes rows of panels with lengths much greater than their heights, resulting in a 2D representation as commonly used in the literature [17–19,30,31].

While the aforementioned models only consider cases when the sun is positioned at the front of the rows, here, the modeling of the direct and circumsolar irradiance shading for all involved surfaces is also included, considering any position of the sun, resulting in a more realistic model. Additionally, the developed model was made generic and can be applied to any first-row transposition model as long as it clearly considers direct, circumsolar, and isotropic irradiance, instead of relying on a predefined first-row model. Extra detail was also included in the modeling of ground shading by considering rows beyond the two main rows being modeled.

The three surfaces considered in this model, namely the front of the panel being evaluated, the back of the panel at its front, and the ground between rows, are divided into segments, as shown in Figure 1, where L, D, h_0, and β are the length of the panels, the horizontal distance between rows, the vertical distance between the ground and the base of the rows, and the tilt angle, respectively. The value of GTI is computed for each segment c of the panel being evaluated and considers the reflected solar irradiance from each segment of the ground u and the back of the front panel v. The number of segments into which these surfaces are divided is defined by the user and can be adjusted, namely the number of segments of the panel being evaluated $i = 1 : n$, the number of segments of the ground $j = 1 : p$, and the number of segments of the back of the front panel $k = 1 : q$.

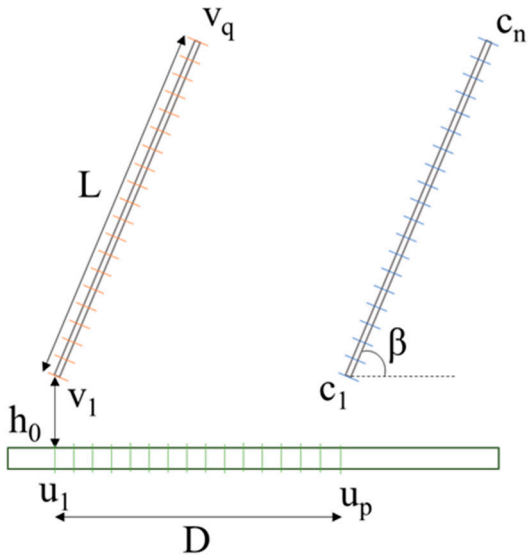

Figure 1. Schematic for modeling GTI in rows that are not the front row.

For each segment of both panels and ground, the GTI is computed as in [19] using Equation (28), where $\vec{GTI}$, $\vec{I}_r$, and $\vec{D}$ are vectors with the values of the global tilted irradiance, the direct normal irradiance, and the diffuse horizontal irradiance, respectively, on each segment of the panel, ground, and front panel. $\boldsymbol{I}$ is the identity matrix while $\boldsymbol{F}$ is the view factor matrix between all segments and $\boldsymbol{R}$ is the reflectivity matrix for each segment. The view factors between all segments are computed using the Hottel crossed string rule [32], and the reflectivity of the front of the panel is assumed to be 0 as in [19].

$$\vec{GTI} = (\boldsymbol{I} - \boldsymbol{FR})^{-1}\left(\vec{I}_r + \vec{D}\right), \tag{28}$$

$$\vec{I}_r = DHI \times \vec{R}_b \tag{29}$$

$$\vec{D} = DIF \times \vec{R}_d \tag{30}$$

$$\vec{R}_b = max\left(0, \frac{cos\,\vec{\theta}}{cos\vec{\Phi}}\right)\left(1 - \vec{S}\right) \tag{31}$$

$$\vec{R}_d = \vec{F}_s X_i + X_{cs}\left(1 - \vec{S}_{cs}\right) \tag{32}$$

For the computation of the transposed direct normal (Equation (29)) and diffuse (Equation (30)) irradiance on each segment, the vectors $\vec{R}_b$ and $\vec{R}_d$ are obtained from Equations (31) and (32) which consist of the tilt factors for the direct (beam) and diffuse irradiances. The shading of the direct irradiance in each segment is taken into consideration

in the direct tilt factor through the vector $\vec{S}$, whose values are either 0, when direct irradiance is not obscured, or 1, when the direct irradiance is obscured, depending on the geometrical characteristics of the installation and the apparent position of the sun in the sky. Regarding the diffuse tilt factor, an isotropic component, X_i, and a circumsolar component, X_{cs}, are modeled as in a first-row transposition model, which, as mentioned above, can be any first-row model as long as it includes direct, circumsolar, and isotropic irradiance components. In the present work, a set of analytical transposition models for first rows are firstly assessed against experimental values and then one is selected, which will then be used in this model evaluation, as reported in the following sections. The sky view factors are computed for each segment considering the summation and reciprocity rules. The fraction of circumsolar irradiance that is obscured is modeled by the vector $\vec{S}_{cs}$ ranging from 0, when there is no obscuration, to 1, when all irradiance from the considered circumsolar region is obscured.

The vectors $\vec{S}$ and $\vec{S}_{cs}$ (Equations (33) and (34), respectively) are determined based on the model proposed by Varga and Mayer [18] with various modifications for the inclusion of cases in which the sun is positioned at the back of the row and the computations for the different segments of the back surface of the row in front of the one being evaluated and the ground. Depending on the surface of each segment, namely the surface of the panel being evaluated, c, the back surface of the panel of the row at its front, v, or the surface of the ground between them, u, the way the shading vectors are modeled differs. Since this is a two-dimensional model, firstly, the projection of the solar elevation angle to the azimuth of the panels, $\alpha\prime$, is needed, which is obtained through Equation (35), where γ_s is the solar azimuth and γ_p is the azimuth of the surfaces.

$$\vec{S} = \begin{bmatrix} \vec{S}_c \\ \vec{S}_u \\ \vec{S}_v \end{bmatrix} \tag{33}$$

$$\vec{S}_{cs} = \begin{bmatrix} \vec{S}_{cs,c} \\ \vec{S}_{cs,u} \\ \vec{S}_{cs,v} \end{bmatrix} \tag{34}$$

$$\alpha\prime = \tan^{-1}\left(\frac{\tan\alpha}{\cos\left(\gamma_s - \gamma_p\right)}\right) \tag{35}$$

The shading of direct beam and the fraction of obscured circumsolar irradiance are determined for each segment of the panel, ground, and back of the front panel according to the projected solar elevation angle relative to each of the angles shown in Figure 2. These angles are computed using Equations (36)–(43), where i, j, and k are the indices of the segments in the panel being evaluated, at the back of the front panel, and on the ground between the rows of panels, respectively. The angles with subscript c are obtained for each segment of the panel being evaluated, those with subscript v are obtained for each segment of the back of the front panel, and those with subscript u are obtained for each segment of ground between the two rows. The angles δ and ε result from the view of the top of an adjacent panel from a segment, the angles ζ and ξ result from the view of the bottom of an adjacent panel from a ground segment, and the angles λ and σ result from the view of the top of a subsequent panel from a ground segment.

$$\delta_c(i) = \tan^{-1}\left[\frac{\left(L - \frac{c(i+1)-c(i)}{2}\right)\sin\beta}{D + \left(\frac{c(i+1)-c(i)}{2} - L\right)\cos\beta}\right] \Pi a = 1, \tag{36}$$

$$\delta_v(k) = \tan^{-1}\left[\left(\frac{\left(L - \frac{v(k+1)-v(k)}{2}\right)\sin\beta}{D}\right)\right] \quad (37)$$

$$\delta_u(j) = \tan^{-1}\left[\frac{L\sin\beta + h_0}{\frac{u(j+1)-u(j)}{2} - L\cos\beta}\right] \quad (38)$$

$$\varepsilon_u(j) = \tan^{-1}\left[\frac{L\sin\beta + h_0}{D - \frac{u(j+1)-u(j)}{2} + L\cos\beta}\right] \quad (39)$$

$$\zeta_u(j) = \tan^{-1}\left[\frac{h_0}{\frac{u(j+1)-u(j)}{2}}\right] \quad (40)$$

$$\lambda_u(j) = \tan^{-1}\left[\frac{L\sin\beta + h_0}{D + \frac{u(j+1)-u(j)}{2} - L\cos\beta}\right] \quad (41)$$

$$\xi_u(j) = \tan^{-1}\left[\frac{h_0}{D - \frac{u(j+1)-u(j)}{2}}\right] \quad (42)$$

$$\sigma_u(j) = \tan^{-1}\left[\frac{L\sin\beta + h_0}{2D - \frac{u(j+1)-u(j)}{2} + L\cos\beta}\right] \quad (43)$$

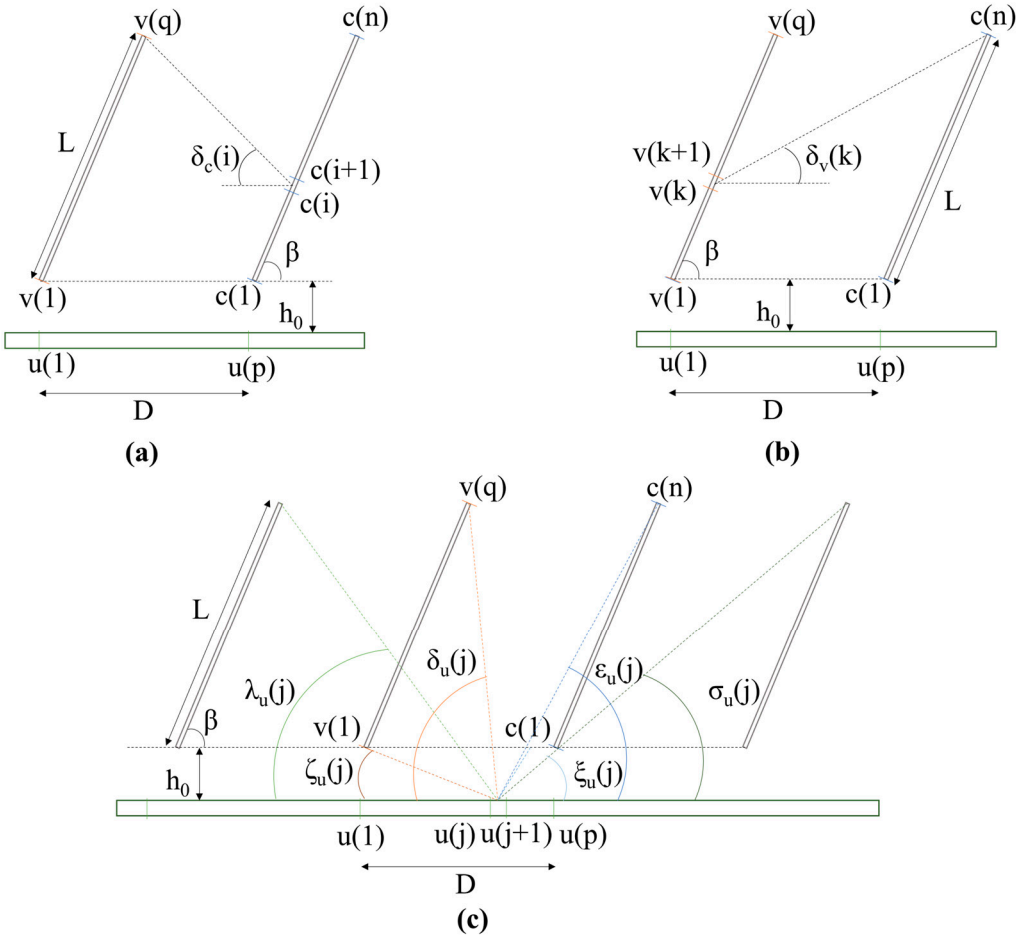

Figure 2. Schematic of the various angles for the computation of shadows and obscuring of circumsolar radiation for (**a**) a segment of the panel being evaluated, (**b**) the back of the front panel, and (**c**) the ground between the rows of panels.

The shading of direct irradiance for each segment of the panel surface, i, is given by Equation (44). Shading can occur ($S_c(i) = 1$) when the sun is positioned either in front of or behind the rows. Specifically, shading occurs when the projected solar elevation angle is positive and lower than the angle from the middle of the segment to the top of the front row (indicating that the sun is behind the front row), or when the projected solar elevation angle is negative and lower than the tilt angle of the surfaces (indicating that the sun is behind the panel). For the remaining cases, the segments are not shaded.

$$S_c(i) = \begin{cases} 1, & \left[\delta_c(i) > \alpha' \wedge \left|\gamma_s - \gamma_p\right| < 90^\circ\right] \vee \left(\beta > |\alpha'| \wedge \left|\gamma_s - \gamma_p\right| \geq 90^\circ\right) \\ 0, & \left[\delta_c(i) \leq \alpha' \wedge \left|\gamma_s - \gamma_p\right| < 90^\circ\right] \vee \left(\beta \leq |\alpha'| \wedge \left|\gamma_s - \gamma_p\right| \geq 90^\circ\right) \end{cases} \quad (44)$$

The shading of direct irradiance for each segment of the back surface of the front row, denoted by index k, is computed through Equation (45). Each segment is always shaded if the sun is positioned in front of the rows. Additionally, if the sun is not in front of the rows, shading occurs when the projected solar elevation angle exceeds the tilt angle of the surfaces or when it is lower than the angle from the middle of the segment to the top of the panel being evaluated.

$$S_v(k) = \begin{cases} 1, & \left|\gamma_s - \gamma_p\right| < 90^\circ \vee \left(\left|\gamma_s - \gamma_p\right| \geq 90^\circ \wedge [\delta_v(k) > |\alpha'| \vee \beta < |\alpha'|]\right) \\ 0, & \left|\gamma_s - \gamma_p\right| \geq 90^\circ \wedge \delta_v(k) \leq |\alpha'| \wedge \beta \geq |\alpha'| \end{cases} \quad (45)$$

The computation of the shading of direct irradiance on the ground between the rows is performed through Equation (46), which involves comparing the projected solar elevation angle with six other angles as depicted in Figure 2 and calculated through Equations (38) to (43).

Each ground segment, denoted by index j, is shaded under the following conditions: when the sun is positioned in front of the rows and behind the row in front, or when its projected solar elevation angle is lower than the angle of the middle of the segment to the top of the subsequent row in front. Additionally, ground segments are shaded if the sun is behind the row being evaluated or when the projected solar elevation angle is lower than the angle from the middle of the segment to the top of the subsequent row behind. Moreover, for ground segments positioned below the front row, shading occurs when the projected solar elevation angle exceeds the tilt of the surfaces.

$$S_u(j) = \begin{cases} 1, & \left|\gamma_s - \gamma_p\right| < 90^\circ \wedge ([\zeta_u(j) < \alpha' < \delta_u(j) \wedge \delta_u(j) > 0] \vee \ \lambda_u(j) > \alpha' \vee [\delta_u(j) \leq 0 \wedge \alpha' > \zeta_u(j)]) \vee \\ & \left|\gamma_s - \gamma_p\right| \geq 90^\circ \wedge \begin{pmatrix} [\varepsilon_u(j) > \xi_u(j) \wedge \varepsilon_u(j) > |\alpha'| > \xi_u(j)] \vee [\varepsilon_u(j) \leq \xi_u(j) \wedge \varepsilon_u(j) < |\alpha'| < \xi_u(j)] \vee \\ [\delta_u(j) < 0 \wedge \ |\delta_u(j)| < |\alpha'|] \vee |\alpha'| \leq \sigma_u(j) \end{pmatrix} \\ 0, & \left|\gamma_s - \gamma_p\right| < 90^\circ \wedge ([\delta_u(j) \geq 0 \wedge \delta_u(j) \leq \alpha'] \vee \ [\lambda_u(j) \leq \alpha' \leq \zeta_u(j)]) \vee \\ & \left|\gamma_s - \gamma_p\right| \geq 90^\circ \wedge \begin{pmatrix} [\delta_u(j) \geq 0 \wedge \varepsilon_u(j) \leq |\alpha'| \wedge \xi_u(j) \leq |\alpha'|] \vee \ [\sigma_u(j) \leq |\alpha'| \leq \xi_u(j) \wedge |\alpha'| \leq \varepsilon_u(j)] \vee \\ [\delta_u(j) < 0 \wedge \ \varepsilon_u(j) \leq |\alpha'| \wedge \xi_u(j) \leq |\alpha'| \wedge |\delta_u(j)| \geq |\alpha'|] \end{pmatrix} \end{cases} \quad (46)$$

The modeling of the circumsolar irradiance obscuring follows a similar approach, albeit with the utilization of the vector $\vec{S}_{cs}$ to represent the fraction of circumsolar irradiance that is obscured. Circumsolar irradiance is assumed as being uniformly distributed within the annular region surrounding the sun disk, with an apparent external angular radius, r, of 15°. The obscured area of the circumsolar region is given by Equation (47) as in [18]:

$$C(x) = \frac{sin^{-1}\frac{\sqrt{r^2 - (|\alpha'| - x)^2}}{r}}{180} - \frac{\sqrt{r^2 - (|\alpha'| - x)^2}}{2\pi r} \quad (47)$$

In the case of the segments of the panel being evaluated (Equation (48)), several conditions dictate the obscuring of circumsolar irradiance. When the sun is positioned in front of the rows, total obscuration ($S_{cs,c}(i) = 1$) occurs if the entire circumsolar region is below the angle defined by the middle of the segment to the top of the front row, denoted as $\delta_c(i)$. Substantial obscuration (more than 50%, $S_{cs,c}(i) = |1 - C(\delta_c(i))|$) occurs

if this angle is higher than the projected solar elevation angle and the difference between these two angles is smaller than the angular radius. It is less obscured (less or equal to 50%, $S_{cs,c}(i) = C(\delta_c(i))$) if the projected solar elevation angle is higher than $\delta_c(i)$ and the difference between these two angles is smaller than the angular radius. Finally, no obscuration ($S_{cs,c}(i) = 0$) occurs if the projected solar elevation angle exceeds $\delta_c(i)$ and the difference between these two angles is higher than the angular radius. A similar principle applies when the sun is behind the rows, with the difference that instead of using the angle $\delta_c(i)$, the comparison is made with the tilt angle β.

$$S_{cs,c}(i) = \begin{cases} 1, & \left[\left|\gamma_s - \gamma_p\right| < 90^\circ \wedge \alpha' - \delta_c(k) \leq -r\right] \vee \left(\left|\gamma_s - \gamma_p\right| \geq 90^\circ \wedge |\alpha'| - \beta \leq -r\right) \\ |1 - C(\delta_c(i))|, & \left|\gamma_s - \gamma_p\right| < 90^\circ \wedge -r < \alpha' - \delta_c(i) < 0 \\ |1 - C(\beta)|, & \left|\gamma_s - \gamma_p\right| \geq 90^\circ \wedge -r < |\alpha'| - \beta < 0 \\ C(\delta_c(i)) & \left|\gamma_s - \gamma_p\right| < 90^\circ \wedge 0 \leq \alpha' - \delta_c(i) < r \\ C(\beta), & \left|\gamma_s - \gamma_p\right| \geq 90^\circ \wedge 0 \leq |\alpha'| - \beta < r \\ 0, & \left[\left|\gamma_s - \gamma_p\right| < 90^\circ \wedge \alpha' - \delta_c(i) \geq r\right] \vee \left(\left|\gamma_s - \gamma_p\right| \geq 90^\circ \wedge |\alpha'| - \beta \geq r\right) \end{cases} \quad (48)$$

The fraction of circumsolar irradiance obscured for each segment of the back surface of the front panels is given by Equation (49). It is assumed that all circumsolar irradiance is obscured when the sun is positioned in front of the rows. When the sun is positioned behind the rows, the projected solar elevation angles plus or minus the circumsolar angular radius are compared in a similar manner to Equation (48), but with reference to the tilt angle of the surface and the angle of the middle of the back surface segment to the top of the panel being evaluated.

$$S_{cs,v}(k) = \begin{cases} 1, & \left(\left|\gamma_s - \gamma_p\right| < 90^\circ\right) \vee \left(\left|\gamma_s - \gamma_p\right| \geq 90^\circ \wedge [|\alpha'| - \delta_v(k) \leq -r \vee |\alpha'| - \beta \geq r]\right) \\ |1 - C(\delta_v(k))|, & \left|\gamma_s - \gamma_p\right| \geq 90^\circ \wedge -r < |\alpha'| - \delta_v(k) < 0 \\ |1 - C(\beta)|, & \left(\left|\gamma_s - \gamma_p\right| \geq 90^\circ \wedge 0 < |\alpha'| - \beta < r\right) \\ C(\delta_v(k)) & \left|\gamma_s - \gamma_p\right| \geq 90^\circ \wedge 0 \leq |\alpha'| - \delta_v(k) < r \\ C(\beta), & \left(\left|\gamma_s - \gamma_p\right| \geq 90^\circ \wedge -r < |\alpha'| - \beta \leq 0\right) \\ 0, & \left[\left|\gamma_s - \gamma_p\right| \geq 90^\circ \wedge |\alpha'| - \delta_v(k) \geq r \wedge |\alpha'| - \beta \leq -r\right] \end{cases} \quad (49)$$

The computation of circumsolar irradiance obscuration for each segment of the ground between rows is more complex (Equation (50)). Complete obscuration is assumed when the entire circumsolar region is positioned either behind the front row panel or the panel being evaluated, considering the middle of the ground segment. Additionally, complete obscuration occurs when the angle of the top of the circumsolar region is lower than the angle of the top of the subsequent rows of panels, whether in front or behind. Similarly to the equations above (Equations (48) and (49)), the projected solar elevation angles plus or minus the circumsolar angular radius are compared with the six different angles shown in the scheme at the bottom of Figure 2 for the computation of the fraction of circumsolar irradiance that is obscured.

$$S_{cs,u}(j) = \begin{cases} 1, & \left[\left|\gamma_s-\gamma_p\right| < 90^\circ \wedge \left(\begin{array}{l}[\delta_u(j) \geq 0 \wedge \alpha' - \zeta_u(j) \geq r \wedge \alpha' - \delta_u(j) \leq -r]\vee \\ \alpha' - \lambda_u(j) \leq -r\vee \\ [\delta_u(j) < 0 \wedge \alpha' - \zeta_u(j) \geq r]\vee \\ [\alpha' - r \leq \lambda_u(j) \wedge \alpha' + r \geq \zeta_u(j)]\end{array}\right)\right]\vee \\ & \left[\left|\gamma_s-\gamma_p\right| \geq 90^\circ \wedge \left(\begin{array}{l}[|\alpha'| - \xi_u(j) \geq r \wedge |\alpha'| - \varepsilon_u(j) \leq -r]\vee \\ |\alpha'| - \sigma_u(j) \leq -r\vee \\ [\delta_u(j) \leq 0 \wedge |\alpha'| - |\delta_u(j)| \geq r]\vee \\ [|\alpha'| - r \leq \sigma_u(j) \wedge |\alpha'| + r \geq \varepsilon_u(j)]\vee \\ [|\alpha'| - r \leq \sigma_u(j) \wedge |\alpha'| + r \geq \xi_u(j)]\end{array}\right)\right] \\ |1 - C(|\delta_u(j)|)|, & \left[\left|\gamma_s-\gamma_p\right| < 90^\circ \wedge \delta_u(j) \geq 0 \wedge -r < \alpha' - \delta_u(j) < 0\right]\vee \\ & \left[\left|\gamma_s-\gamma_p\right| \geq 90^\circ \wedge \delta_u(j) < 0 \wedge 0 \leq |\alpha'| - |\delta_u(j)| < r\right] \\ |1 - C(\varepsilon_u(j))|, & \left|\gamma_s-\gamma_p\right| \geq 90^\circ \wedge -r < |\alpha'| - \varepsilon_u(j) < 0 \\ |1 - C(\zeta_u(j))|, & \left|\gamma_s-\gamma_p\right| < 90^\circ \wedge \alpha' - r > \lambda_u(j) \wedge 0 < \alpha' - \zeta_u(j) < r \\ |1 - C(\lambda_u(j))|, & \left|\gamma_s-\gamma_p\right| < 90^\circ \wedge \alpha' + r < \zeta_u(j) \wedge -r < \alpha' - \lambda_u(j) < 0 \\ |1 - C(\xi_u(j))| & \left|\gamma_s-\gamma_p\right| \geq 90^\circ \wedge |\alpha'| - r > \sigma_u(j) \wedge 0 < |\alpha'| - \xi_u(j) < r \\ |1 - C(\sigma_u(j))|, & \left|\gamma_s-\gamma_p\right| \geq 90^\circ \wedge |\alpha'| + r < \xi_u(j) \wedge -r < |\alpha'| - \sigma_u(j) < 0 \\ C(|\delta_u(j)|) & \left[\left|\gamma_s-\gamma_p\right| < 90^\circ \wedge \delta_u(j) \geq 0 \wedge 0 \leq \alpha' - \delta_u(j) < r\right]\vee \\ & \left[\left|\gamma_s-\gamma_p\right| \geq 90^\circ \wedge \delta_u(j) < 0 \wedge -r \leq |\alpha'| - |\delta_u(j)| < 0\right] \\ C(\varepsilon_u(j)), & \left|\gamma_s-\gamma_p\right| \geq 90^\circ \wedge 0 \leq |\alpha'| - \varepsilon_u(j) < r \\ C(\zeta_u(j)), & \left|\gamma_s-\gamma_p\right| < 90^\circ \wedge \alpha' - r > \lambda_u(j) \wedge -r < \alpha' - \zeta_u(j) < 0 \\ C(\lambda_u(j)), & \left|\gamma_s-\gamma_p\right| < 90^\circ \wedge \alpha' + r < \zeta_u(j) \wedge 0 < \alpha' - \lambda_u(j) < r \\ C(\xi_u(j)), & \left|\gamma_s-\gamma_p\right| \geq 90^\circ \wedge |\alpha'| - r > \sigma_u(j) \wedge -r < |\alpha'| - \xi_u(j) < 0 \\ C(\sigma_u(j)), & \left|\gamma_s-\gamma_p\right| \geq 90^\circ \wedge |\alpha'| + r < \xi_u(j) \wedge 0 < |\alpha'| - \sigma_u(j) < r \\ 0, & \left[\left|\gamma_s-\gamma_p\right| < 90^\circ \wedge \left(\begin{array}{l}[\delta_u(j) \geq 0 \wedge \alpha' - \delta_u(j) \geq r]\vee \\ [\alpha' - \zeta_u(j) \leq -r \wedge \alpha' - \lambda_u(j) \geq r]\end{array}\right)\right]\vee \\ & \left[\left|\gamma_s-\gamma_p\right| \geq 90^\circ \wedge \left(\begin{array}{l}|\alpha'| - \varepsilon_u(j) \geq r\vee \\ [|\alpha'| - \xi_u(j) \leq -r \wedge |\alpha'| - \sigma_u(j) \geq r \wedge |\alpha'| - \varepsilon_u(j) \leq -r]\end{array}\right)\right] \end{cases} \quad (50)$$

4. Experimental Setup and Procedure

In order to obtain observational data for both a first row and subsequent rows of panels with varying tilt angles and inter-row distances, a structure featuring a pyranometer for measuring GTI was constructed in an open field near Évora, Portugal (38.5306°, −8.0112°), as shown in Figures 3–5.

The experimental setup consists of three frames: a base, a front frame, and a rear frame, with a pyranometer installed on the rear frame. The base was leveled, and two transversal bars on the sides ensured that both front and rear frames maintained the same tilt angle. The apparatus allows for adjustment with three degrees of freedom: tilt angle of the front and rear frames (β, from 20° to 90°) through the solidary adjustment of the inclination of both frames; distance between frames (D, from 0.80 m to 1.10 m) through three positions of where the front frame can be fixed to the base; and position of the pyranometer along the length of the rear frame (c_s, from 0.08 m to 1.08 m) by sliding the instrument along its supporting bar. The uncertainty on the measurements of each of these variables is 1 cm in the cases of distances and 1° in the case of the tilt angles.

To represent the adjacent row, three Alveopan bilaminate white polypropylene boards, with a total width W of 3.03 m and length L of 1.08 m, were installed in the front frame. The reflectivity of these boards was measured using a FieldSpec HandHeld 2 spectroradiometer (ASD, Inc., Boulder, CO, USA) [33], yielding an average reflectivity of 0.921. Although potential edge effects were acknowledged due to board sizes, these were not factored into the general model. For data collection purposes relevant to the assessment of transposition models applied to the first rows, these boards were removed.

Figure 3. Experimental setup for measuring global tilt irradiance for different positions.

Figure 4. Overview of the experimental setup including (**a**) the Évora–PECS station and (**b**) the pyranometers used for albedo computations.

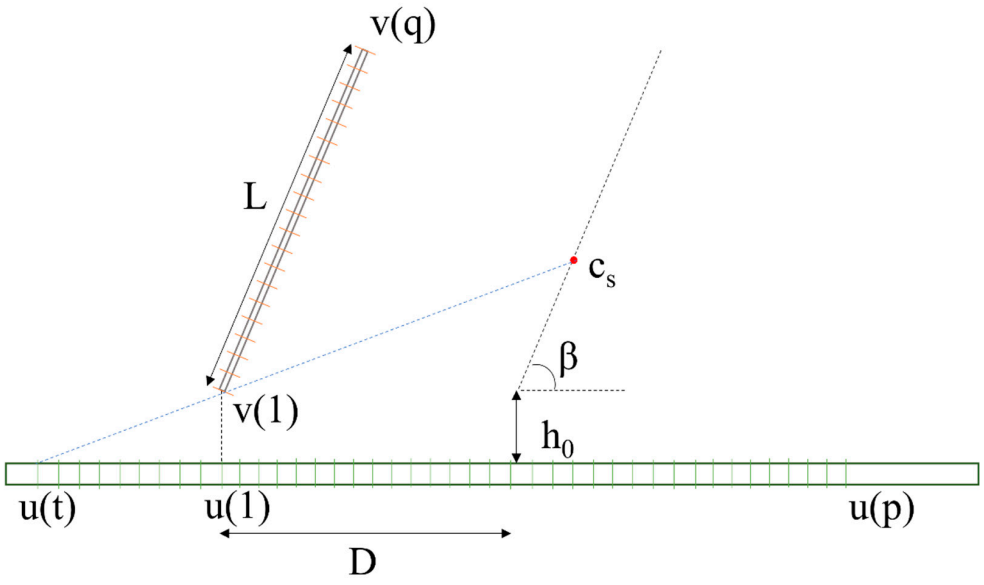

Figure 5. Schematic for modeling GTI on the sensor in the experimental apparatus.

Global tilted irradiance was measured using a Kipp & Zonen CMP11 pyranometer (Kipp & Zonen, Delft, The Netherlands), while global horizontal irradiance and reflected

irradiances (for the computation of ground albedo) were measured using a Kipp & Zonen CM7B albedometer (Kipp & Zonen, Delft, The Netherlands). Both sensors were connected to a CR300 datalogger from Campbell Scientific (Shepshed, Loughborough, UK). Additionally, DNI, DIF, and GHI observation data were obtained from the Évora–PECS station of the DNI-ALENTEJO project network [34], located 5 m from the experimental setup.

The internal clock of the CR300 data logger used in the apparatus was synchronized with the data logger of the Évora–PECS station, both set to UTC time. Sensor outputs were sampled at 1 Hz and mean, maximum, minimum, and standard deviation values were recorded every minute. Observations were corrected following the best practices in the field, namely the WMO recommendations and the BSRN (Baseline Solar Radiation Network) guide, including corrections for sensor zero offset and filters according to the BSRN quality control procedure, considering the extremely rare limits [35] and removing measurements for zenith angles equal or above 85°.

Prior to the field measurements, a calibration procedure was conducted specifically for the CMP11 pyranometer and CM7B albedometer using a reference CMP21 pyranometer (Kipp & Zonen, Delft, The Netherlands), according to the ISO 9847:1992 standard [36].

For the accurate application of transposition models, the ground albedo value is needed. While a standard value of 0.2 is often used, this study estimated the ground albedo using Equation (51) [37], where BSA and WSA represent the black-sky albedo and white-sky albedo, respectively. BSA is defined as the albedo in the absence of the diffuse component and is a function of the solar zenith angle, while the WSA is the albedo considering the diffuse component as isotropic and in the absence of the direct component. The mean values of BSA and WSA were obtained by fitting Equation (44) to experimental data, where the albedo, ρ, was computed by applying the ratio of reflected (GRI) to global horizontal (GHI) irradiance observations from the albedometer. Following data treatment, including filtering and removal of the records for solar zenith angles lower than 70°, BSA and WSA were found to be 0.206 and 0.208, respectively, across all recorded data periods.

$$\rho = BSA + (WSA - BSA)\frac{DIF}{GHI} \tag{51}$$

Observations were conducted between 14 April and 1 June 2022. For first-row tests, 5 datasets or periods were generated, each corresponding to a specific tilt angle, as shown in Table 1, with the pyranometer positioned at c_s = 0.50 m. Testing of the developed model for other rows resulted in 19 periods with various tilt angles, distance between rows, and pyranometer positions, as shown in Table 2. Periods 4, 9, and 19 include instances in which the pyranometer is shaded.

It should be noted that measurements were conducted during a period of relatively high solar elevation, minimizing shading effects. To better capture shading effects, the inter-row distance during experimental tests were shorter than typical photovoltaic power plant configurations. Nonetheless, the developed model is designed to encompass diverse real-world conditions in the field.

Table 1. Structure position and number of 1 min data points for each testing period of the first-row tests.

Period	β (°)	Number of Data Points
1	20	551
2	38	582
3	50	620
4	70	545
5	90	508
All	-	2806

Table 2. Structure position and number of 1 min data points for each testing period of the proposed model for rows other than the first.

Period	D (m)	β (°)	c_s (m)	Number of Data Points
1	1.10	38	0.08	585
2	1.10	38	0.58	604
3	1.10	38	1.08	1528
4	0.81	38	0.18	2345
5	0.81	38	0.38	605
6	0.81	38	0.58	615
7	0.81	38	0.78	608
8	0.81	38	0.98	585
9	0.80	50	0.15	581
10	0.80	50	0.35	2412
11	0.80	50	0.55	617
12	0.80	50	0.75	632
13	0.80	50	0.95	651
14	0.84	20	0.26	1807
15	0.84	20	0.46	365
16	0.84	20	0.66	648
17	0.84	20	0.86	612
18	0.84	20	1.06	633
19	0.81	38	0.18	718
All	-	-	-	17,151
Shaded	-	-	-	2163
Unshaded	-	-	-	14,988

5. Results and Discussion

The different transposition models, including the developed model for rows that are not the first, were applied to the observations of DNI and DIF from the Évora–PECS station. Subsequently, the model outputs were compared with GTI observations from the experimental setup using multiple evaluation metrics developed in the software MATLAB R2018b. These metrics comprised the coefficient of determination (R^2), mean bias error (MBE), and root-mean-squared error (RMSE) along with a global performance index (GPI) based on R^2, MBE, and RMSE, where a higher value represents the better accuracy of the model [22].

Given the significant influence of atmospheric conditions, particularly cloud cover, on global irradiance, the mean and standard deviation of the clearness index were computed for each period based on 1 min observations. The clearness index, typically ranging from 0 to 1, represents the ratio of global horizontal irradiance measured at ground level to its counterpart estimated at the top of the atmosphere [34] (Equation (15)). It serves as an indicator of the total transmittance of the atmosphere, reflecting higher values under clear-sky conditions and lower values under overcast conditions. The subsequent subsections provide detailed tables presenting these clearness index values for each period.

Some clearness index values exceeded unity, with a maximum value of 1.079, attributed to cloud enhancement events. These phenomena occur when partly cloudy skies lead to a temporary increase in local GHI above the extraterrestrial irradiance, facilitated by multiple scatterings and reflections by clouds [35]. These values were kept in the analysis, as they capture the transient nature of atmospheric conditions during the observation periods.

5.1. Results for the First Row

The transposition models presented in Section 2.1 were computed for the periods shown in Table 1, with the resulting mean and standard deviation of the clearness index and GTI, alongside various evaluation metrics, summarized in Table 3. Across all models, GTI values were generally underestimated, with the exception of the Bugler and Modified Bugler models, where GTI was overestimated. This discrepancy could stem from the

treatment of the direct normal component within the factor R_b used for modeling the diffuse component. Nevertheless, the Modified Bugler model showed better results compared with the other models. The Modified Bugler model tends to perform best except for vertical surfaces (period 5), where the Klucher model seems to show better results. Given that the global performance index (GPI) for the overall data presented the Modified Bugler model as the best performing model, it was chosen as the primary model for first-row applications in the proposed model. Despite its tendency to overestimate GTI, with an overall MBE of 23.8 W/m^2 and RMSE of 30.5 W/m^2, it delivered optimal results for period 3, characterized by a tilt angle of 50° and small variation in sky conditions (standard deviation of clearness index of 0.087).

Table 3. Mean and standard deviation of the clearness index and GTI and metrics of GTI from the transposition models analyzed for each and all measuring periods of the first-row tests. The best performing model is represented in bold for each indicator and period and the clearness index data are repeated for each metric for better readability.

Metric	Period	k_t		GTI		Liu Jordan	Klucher	Hay Davies	Reindl	Ma Iqbal	Modified Ma Iqbal	Bugler	Modified Bugler	Temps Coulson	Perez
		Mean	Std	Mean (W/m^2)	Std (W/m^2)										
R^2	1	0.697	0.100	700.0	322.0	0.9995	0.9992	0.9995	0.9995	**0.9995**	0.9995	0.9994	0.9995	0.9987	0.9994
	2	0.720	0.081	702.1	330.0	0.9991	0.9988	0.9991	**0.9992**	0.9991	0.9991	0.9990	0.9991	0.9985	0.9991
	3	0.674	0.087	585.5	297.9	0.9955	0.9941	0.9965	0.9967	0.9959	0.9959	0.9946	0.9957	0.8341	**0.9975**
	4	0.686	0.141	474.8	288.4	**0.9946**	0.9936	0.9945	0.9938	0.9944	0.9944	0.9942	0.9944	0.9317	0.9934
	5	0.676	0.102	327.7	202.8	0.9982	0.9963	0.9978	0.9953	0.9979	0.9978	0.9991	0.9987	0.9837	**0.9993**
	All	0.690	0.105	558.1	323.6	0.9959	0.9969	0.9974	0.9975	0.9970	0.9970	0.9938	0.9947	0.9216	**0.9978**
MBE (W/m^2)	1	0.697	0.100	700.0	322.0	−44.4	**−28.8**	−36.6	−36.4	−38.6	−38.4	58.1	29.8	−43.7	−31.5
	2	0.720	0.081	702.1	330.0	−53.7	−40.7	−44.6	−43.9	−46.9	−46.7	51.2	**23.6**	−34.6	−36.5
	3	0.674	0.087	585.5	297.9	−66.5	−32.4	−48.6	−42.4	−53.9	−53.5	23.0	**5.3**	−157.4	−24.1
	4	0.686	0.141	474.8	288.4	−51.4	−28.4	−45.1	−38.4	−46.5	−46.5	37.2	**19.7**	−75.0	−24.0
	5	0.676	0.102	327.7	202.8	−23.2	**−2.0**	−27.3	−18.3	−25.8	−26.2	57.9	44.6	−19.6	−10.3
	All	0.690	0.105	558.1	323.6	−48.7	−27.1	−40.9	−36.4	−42.9	−42.8	44.8	**23.8**	−68.7	−25.6
RMSE (W/m^2)	1	0.697	0.100	700.0	322.0	49.7	36.1	41.3	41.2	43.5	43.3	59.1	**30.4**	45.8	37.5
	2	0.720	0.081	702.1	330.0	56.1	43.5	46.3	45.6	48.8	48.5	53.9	**25.8**	36.1	38.9
	3	0.674	0.087	585.5	297.9	71.9	38.0	51.7	45.1	57.6	57.2	27.4	**15.2**	181.8	26.9
	4	0.686	0.141	474.8	288.4	56.5	34.8	48.7	42.7	50.4	50.3	42.9	**26.7**	94.8	30.8
	5	0.676	0.102	327.7	202.8	24.9	11.8	28.3	21.7	27.0	27.3	62.6	48.2	41.9	11.3
	All	0.690	0.105	558.1	323.6	54.9	35.0	44.5	40.7	47.1	47.0	50.2	**30.5**	100.2	30.9
GPI	All	0.690	0.105	558.1	323.6	1.068	1.848	1.412	1.569	1.324	1.329	1.195	**1.959**	−1.000	1.953

5.2. Results for Other Rows

For the evaluation of the developed transposition model for rows other than the first, some adjustments were implemented to accommodate the experimental setup (refer to Figure 5). Given the absence of panels in the second row, this row was not considered in the modeling. Instead, *GTI* was computed for each segment of the back of the front panel and ground, followed by the calculation of *GTI* at a designated point which represents the sensor. In this case, the angles ε_u, λ_u, ξ_u, σ_u, and δ_v used for shadow computation and circumsolar irradiance obscuration were not applicable. Another modification involved the length of ground considered in the model. Since the setup comprised only one panel, reflections from the ground beyond the modeled rows could significantly impact the measured GTI and were thus incorporated into the model validation process (depicted in Figure 5).

GTI estimation was performed using both the developed model and the Modified Bugler model for reference and comparison, which is a common practice in the absence of a specific model for other rows. It is important to note that the configurations used in

periods 4, 9, and 19 result in direct shading of the pyranometer for a certain time span of the day. As example, periods 1 and 12, when there was no shading, and period 19, when there was shading and obscuration of the pyranometer by the front row, are shown in Figures 6–8 (the small data gaps during the day are a result of the filtering procedure mentioned in Section 4). Despite the fact that slightly lesser improvements are observed for period 12 (Figure 6), which is attributed to partially cloudy conditions, the effectiveness of the developed model over the Modified Bugler is evident across the evaluated periods.

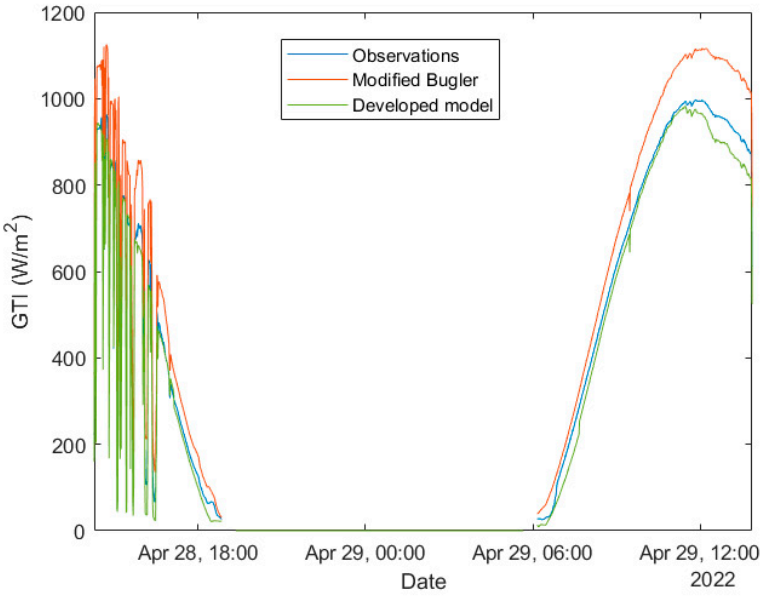

Figure 6. Global tilted irradiance observed and modeled by the Modified Bugler model (first-row model for reference and comparison) and the developed model for period 1 (1 min timestep).

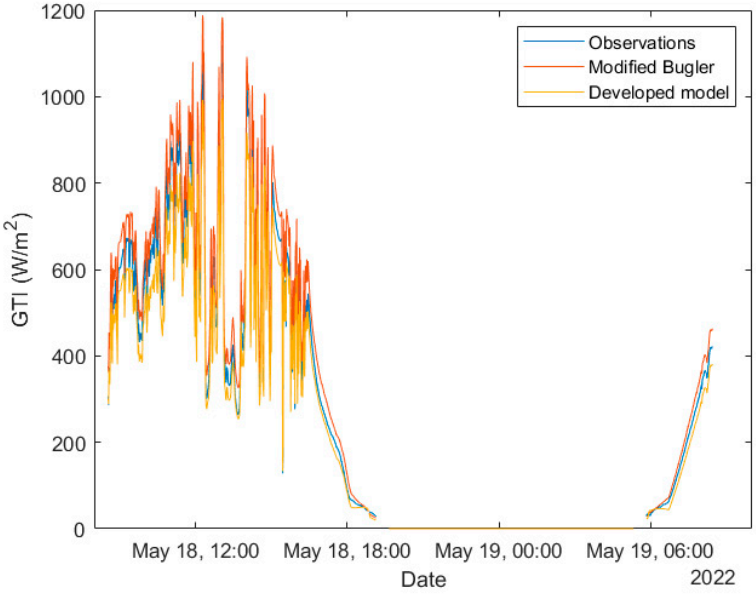

Figure 7. Global tilted irradiance observed and modeled by the Modified Bugler model (first-row model for reference and comparison) and the developed model for period 12 (1 min timestep).

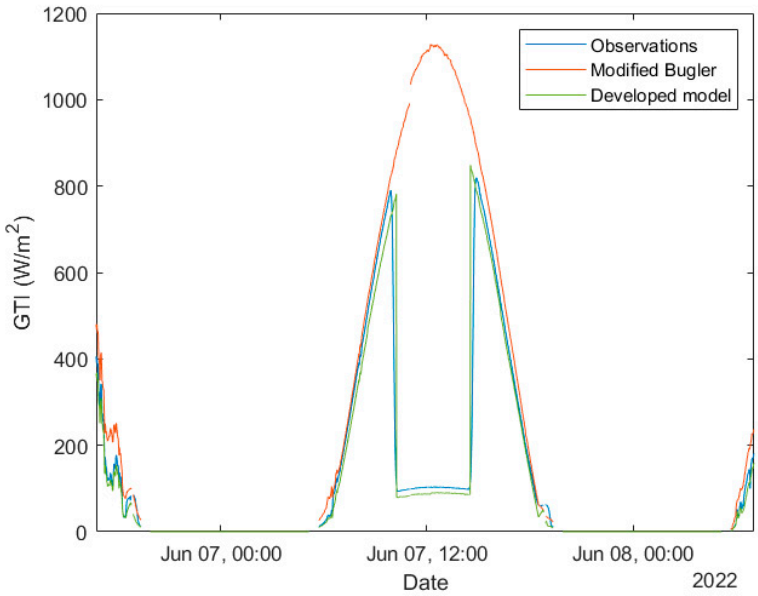

Figure 8. Global tilted irradiance observed and modeled by the Modified Bugler model (first-row model for reference and comparison) and the developed model for period 19 (1 min timestep).

The results for each period, all periods, and for the data when the pyranometer is shaded or unshaded are presented in Table 4. When compared with the original Modified Bugler model, which overestimates the GTI, the proposed model improves the MBE for most periods, albeit with a slight underestimation. Typically, the Modified Bugler performs better in periods characterized by higher pyranometer positioning and greater frame-to-frame distances, resembling first-row irradiance conditions. During periods of direct irradiance shading (periods 4, 9, and 19), the Modified Bugler model, which does not consider shading, shows significantly higher errors. Another aspect to highlight is the impact of clouds in the performance of the model. In periods 9 and 14, for example, when the mean clearness index is lower and its standard deviation is higher (indicating cloudier skies) the metrics show lower performance of both models.

Table 4. Mean and standard deviation of the clearness index and metrics of GTI from the Modified Bugler model and proposed model for other rows.

Period	k_t		GTI		Modified Bugler Model			Developed Model for Other Rows		
	Mean	Std	Mean (W/m^2)	Std (W/m^2)	R^2	MBE (W/m^2)	RMSE (W/m^2)	R^2	MBE (W/m^2)	RMSE (W/m^2)
1	0.687	0.077	566.1	342.1	0.9905	100.0	106.1	0.9921	−31.1	39.5
2	0.675	0.108	646.2	324.4	0.9988	75.6	76.6	0.9987	−38.5	44.8
3	0.584	0.204	456.2	338.0	0.9413	57.9	96.2	0.9410	−24.7	82.0
4	0.641	0.191	176.2	126.3	0.0873	521.5	651.9	0.9844	−15.7	22.7
5	0.704	0.095	627.8	335.9	0.9984	76.4	78.5	0.9990	−38.6	42.3
6	0.690	0.103	599.6	356.2	0.9995	68.4	70.8	0.9991	−39.4	42.3
7	0.672	0.098	582.9	345.2	0.9996	69.3	71.0	0.9996	−39.4	43.8
8	0.684	0.104	634.2	335.2	0.9990	36.6	37.6	0.9988	−69.5	77.3
9	0.540	0.206	248.4	187.0	0.1385	290.2	376.0	0.3225	−81.1	161.5
10	0.590	0.190	420.5	307.1	0.9769	103.4	112.0	0.9944	−42.3	50.6
11	0.674	0.145	548.9	307.6	0.9986	61.2	62.1	0.9962	−51.6	57.8
12	0.622	0.157	432.0	270.4	0.9949	52.4	55.2	0.9946	−54.0	62.1
13	0.561	0.134	436.4	272.7	0.9962	37.9	40.6	0.9961	−44.7	58.7
14	0.351	0.192	124.5	79.55	0.4669	250.6	304.9	0.4610	87.0	141.2
15	0.636	0.154	440.7	300.0	0.9980	28.3	30.3	0.9987	−62.7	69.6
16	0.524	0.275	481.7	370.5	0.9792	35.1	61.7	0.9793	−50.3	78.2
17	0.695	0.172	679.9	360.3	0.9907	41.5	50.6	0.9909	−65.9	78.0
18	0.677	0.147	643.9	334.1	0.9966	37.4	42.4	0.9964	−63.4	69.0
19	0.644	0.177	248.6	232.2	0.0372	373.2	570.2	0.9063	−12.4	75.5
All	0.638	0.188	323.8	304.6	0.4698	381.2	301.2	0.9543	−12.9	76.8
Shaded	0.682	0.197	203.7	169.2	0.0028	717.3	775.0	0.2585	−28.9	84.2
Unshaded	0.632	0.186	421.6	336.7	0.9047	88.9	131.0	0.9552	−26.5	75.7

Due to the variation in sky conditions along the different periods, the comparison between the different positioning of the setup proved challenging and thus, more importance is given to the overall results instead of each period. In this regard, the developed model for rows affected by the presence of rows in front showed an MBE of -12.9 W/m^2 and a root-mean-squared error of 76.8 W/m^2. As expected, this model outperforms the first-row model when the pyranometer is shaded. Even under unshaded conditions, the developed model is better than the model for the first row, showing the impact of the obscuring of the sky dome due to the other rows, considering the sky radiance anisotropy, namely the circumsolar region, and of the reflections from the front row and ground on the GTI.

To quantify the impact of the proposed model on reducing the error for each irradiance component on a tilted surface compared with the Modified Bugler model, a weight (w_i) for each component i of GTI was computed through Equation (52):

$$w_i = \frac{1}{n}\sum \frac{i_D - i_{MB}}{GTI_D - GTI_{MB}} \quad (52)$$

Here, D stands for developed model and MB for the Modified Bugler model. The results are presented in Table 5 for the direct, I_b, diffuse circumsolar, D_{cs}, diffuse isotropic, D_{iso}, and reflected, I_{refl}, components and for both unshaded and shaded conditions. For the proposed model, the reflected component includes reflections in the ground and in the back side of the front panel. The mean bias error of each model is also included in the table for reference.

Table 5. MBE and weight of each component of GTI on the reduction in bias error when comparing the developed model with the Modified Bugler model.

Period	MBE Modified Bugler (W/m^2)	MBE Developed Model (W/m^2)	w_{Ib} (%)	w_{Dcs} (%)	w_{Diso} (%)	w_{Irefl} (%)
Unshaded	88.9	−26.5	0.0	0.5	56.6	42.9
Shaded	717.3	−28.9	66.5	2.6	28.7	2.2
All	381.2	−12.9	8.4	0.8	53.1	37.7

Overall, the masking of the isotropic diffuse irradiance has the highest weight in the difference between the Modified Bugler and the developed model followed by the modeling of reflected irradiance. As expected, when the direct irradiance is shaded, this becomes the most impactful component, while for unshaded conditions, it has no impact.

6. Operational Algorithm for Forecasting of Solar Irradiance on Tilted Surfaces

This section presents the application of the developed model to predict irradiance on tilted surfaces using operational direct normal and diffuse irradiance forecasts as inputs.

6.1. Forecast Input Data

The transposition models presented in this work, in particular the developed model for rows that are not the first, require several geometrical details on the solar panels of the power plant as input. However, only two meteorological variables, specifically DNI and DIF, are necessary for the determination of the GTI. The European Centre for Medium-range Weather Forecasts (ECMWF) developed the Integrated Forecasting System (IFS), which issues global hourly forecasts every day at 00 UTC up to 10 days ahead. These forecasts include the GHI and DNI variables, while DIF can be computed through the closure function $GHI = BHI + DIF$ (where BHI is given by Equation (2)).

In the work by Pereira et al. [22], a method based on artificial neural networks (ANNs) was developed to generate improved spatial and temporal downscaled DNI forecasts using operational forecast outputs from the ECMWF/IFS and the Copernicus Atmospheric Monitoring Service (CAMS). This work employs the same models and procedure, while also including the analysis and usage of GHI as compared with previous work. Figures 9–11 pro-

vide a direct comparison between ECMWF/IFS forecasts and observations made through calibrated sensors at Évora–Verney station in Portugal (38.5678, −7.9114). These figures show data for DNI, GHI, and DIF for each forecast day of the forecast horizon (day 0: 1 h to 24 h; day 1: 25 h to 48 h; day 2: 49 h to 72 h) over the period from 1 December 2016 to 31 May 2021, with a timestep of 10 min.

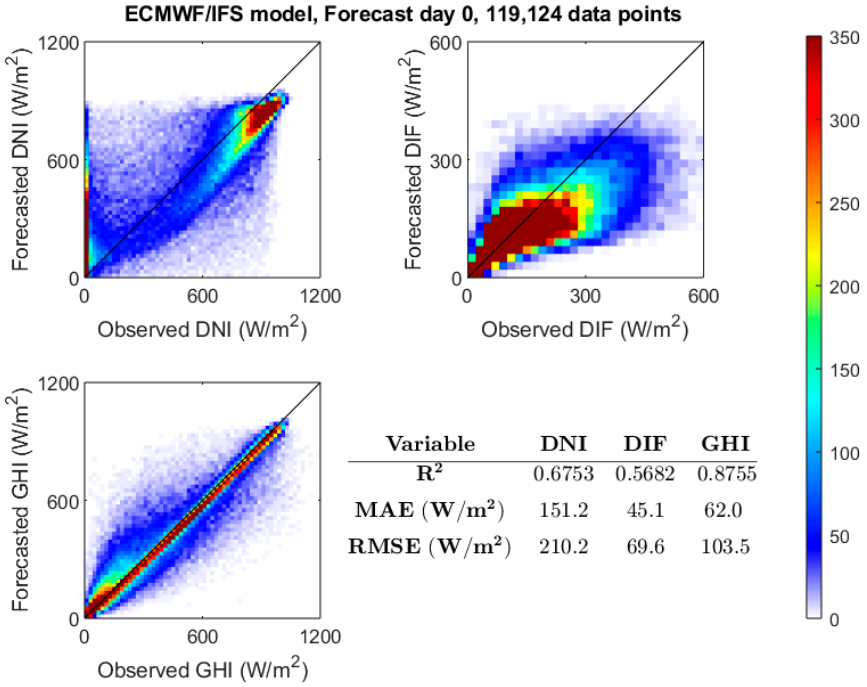

Variable	DNI	DIF	GHI
R^2	0.6753	0.5682	0.8755
MAE (W/m^2)	151.2	45.1	62.0
RMSE (W/m^2)	210.2	69.6	103.5

Figure 9. Comparison between downscaled 10 min forecasts of the ECMWF/IFS and observations made at Évora–Verney of DNI, DIF, and GHI for forecast day 0 (the colormap represents the number of data points in each bin; bin size: 20 × 20 W/m^2).

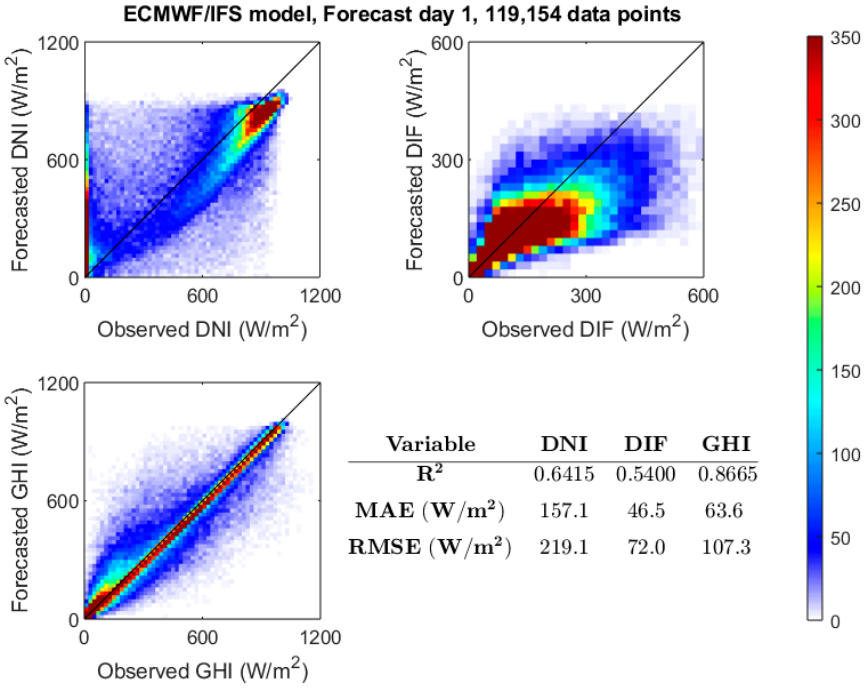

Variable	DNI	DIF	GHI
R^2	0.6415	0.5400	0.8665
MAE (W/m^2)	157.1	46.5	63.6
RMSE (W/m^2)	219.1	72.0	107.3

Figure 10. Comparison between 10 min downscaled forecasts of the ECMWF/IFS and observations made at Évora–Verney of DNI, DIF, and GHI for forecast day 1 (the colormap represents the number of data points in each bin; bin size: 20 × 20 W/m^2).

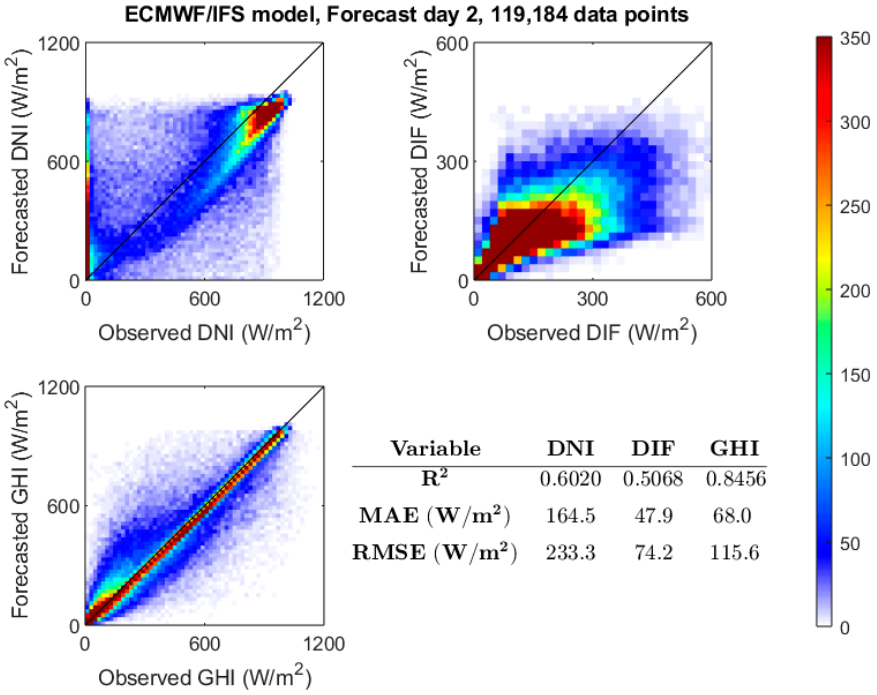

Variable	DNI	DIF	GHI
$\mathbf{R^2}$	0.6020	0.5068	0.8456
$\mathbf{MAE\ (W/m^2)}$	164.5	47.9	68.0
$\mathbf{RMSE\ (W/m^2)}$	233.3	74.2	115.6

Figure 11. Comparison between 10 min downscaled forecasts of the ECMWF/IFS and observations made at Évora–Verney of DNI, DIF, and GHI for forecast day 2 (the colormap represents the number of data points in each bin; bin size: 20 × 20 W/m^2).

As expected, shorter forecast horizons correspond to smaller errors in the forecasts. Improved DNI forecasts were obtained using artificial neural network models, accounting for the nonlinear relationships between the DNI and various meteorological forecasted variables, such as GHI, cloud cover, and aerosol optical depth, as well as the variation in DNI over a given period before the forecasted instant. A brief explanation of this model and procedure can be found in Appendix A. The application of this procedure results in the metrics shown in Figure 12, where the diffuse component was computed using the GHI forecasted by the ECMWF/IFS and the improved DNI forecasts generated by the ANN models.

The application of the ANN model shows improvements in the forecasting of both DNI and DIF over a dataset that encompasses different sky conditions. The same procedure was applied by retrieving weather forecasts for the measurement periods used in this work to evaluate the different transposition models (Section 4). The resulting 10 min improved DNI and computed DIF forecasts were then evaluated against the 10 min mean observations obtained from the experimental data presented in Section 4.

Table 6 shows the results for first-row and inner-row tests. Detailed results for each testing period can be found in Appendix B. Similar to the larger dataset, the longer the forecast horizon, the higher the errors. However, the errors obtained tend to be greater than the ones aforementioned. This discrepancy is due to the smaller dataset used for this analysis, where even minor differences between forecasts and observations can lead to significant errors. Forecasts of DNI and DIF tend to have larger errors compared to global variables such as GHI or GTI, since accurate forecasting of clouds, specifically their location, is critical for this temporal resolution. The GTI results from the transposition models, based on the output of these forecast models, are presented in the following.

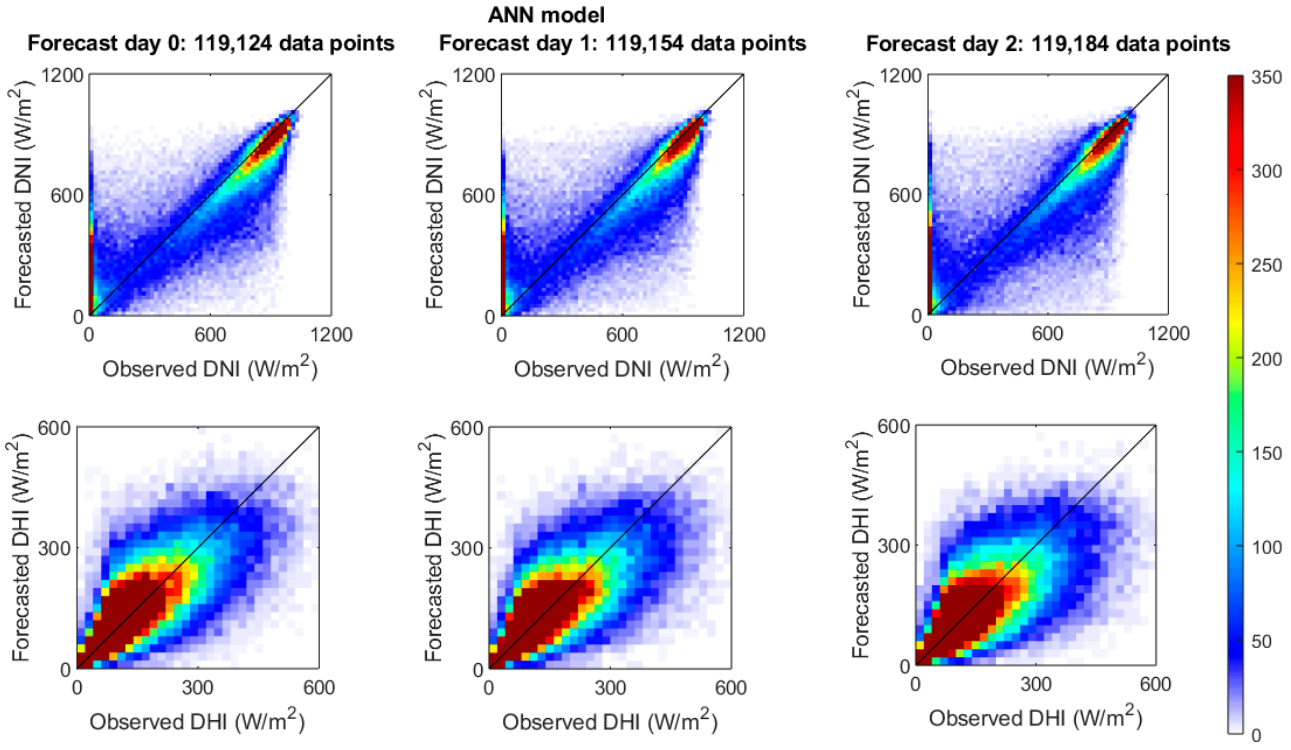

Variable	DNI	DHI
R^2	0.7498	0.6087
MAE (W/m^2)	125.5	42.2
RMSE (W/m^2)	184.4	66.6

Variable	DNI	DHI
R^2	0.7234	0.5883
MAE (W/m^2)	130.9	43.0
RMSE (W/m^2)	193	68.1

Variable	DNI	DHI
R^2	0.6789	0.5475
MAE (W/m^2)	139.2	45.4
RMSE (W/m^2)	209.0	71.8

Figure 12. Comparison between improved 10 min forecasts and observations made at Évora–Verney of DNI and DIF for forecast days 0, 1, and 2 (the colormap represents the number of data points in each bin; bin size: 20 × 20 W/m^2).

Table 6. DNI and DIF forecast results for all data of first-row tests and for all shaded and unshaded data of the developed model testing (MBE, MAE, and RMSE in W/m^2).

Data and Variable		Day 0 R^2	Day 0 MBE	Day 0 MAE	Day 0 RMSE	Day 1 R^2	Day 1 MBE	Day 1 MAE	Day 1 RMSE	Day 2 R^2	Day 2 MBE	Day 2 MAE	Day 2 RMSE
First-row tests													
All	DNI	0.4859	−38.5	87.2	132.1	0.2568	−41.5	107.4	169.2	0.2373	−99.8	151.2	225.7
	DIF	0.5258	−1.6	44.2	62.1	0.5540	4.0	41.3	60.3	0.5382	7.7	48.6	62.4
Inner-row tests													
All	DNI	0.5386	34.0	146.3	208.7	0.5458	39.4	145.1	208.6	0.4930	31.8	156.0	224.6
	DIF	0.4252	66.4	66.5	94.6	0.4720	64.0	64.0	91.5	0.4316	68.3	68.3	95.2
Shaded	DNI	0.6166	126.4	185.6	267.4	0.6488	134.8	183.6	263.8	0.5840	121.6	196.2	272.8
	DIF	0.4670	−49.7	92.8	126.8	0.5025	−53.1	97.1	126.9	0.4255	−44.4	101.0	131.0
Unshaded	DNI	0.5351	16.9	139.0	196.0	0.5389	21.8	138.0	196.7	0.4876	15.2	148.5	214.6
	DIF	0.3884	−8.9	61.6	87.4	0.4437	−17.6	57.8	83.3	0.4038	−15.6	62.3	87.1

6.2. Operational Analysis of Transposition Models

To understand how the selected transposition models perform in an operational forecast context, the transposition models were applied using the resulting forecasts of DNI and DIF for the testing location with a 10 min timestep. The results were then compared with the observations.

Table 7 presents the results for the first row using the Modified Bugler model and for inner rows using the developed model for each day of the forecast horizon.

Table 7. GTI results of the developed model for rows that are not the front row for each day of forecast horizon using DNI and DIF forecasts (MAE and RMSE in W/m^2; MAPE and RMSPE in %).

Data	Day 0				Day 1				Day 2			
	R^2	MBE	MAE	RMSE	R^2	MBE	MAE	RMSE	R^2	MBE	MAE	RMSE
First-row tests												
All	0.9646	6.7	34.5	48.7	0.9607	15.5	39.4	55.0	0.8001	71.5	67.3	128.5
Inner-row tests												
All	0.7197	−31.5	100.6	164.0	0.7162	−32.1	101.1	165.6	0.6727	−37.2	106.8	179.4
Shaded	0.0074	−115.3	152.4	285.1	0.0242	−116.7	152.4	281.8	0.0078	−113.9	151.3	284.5
Unshaded	0.8031	−16.0	91.0	129.8	0.7907	−16.5	91.6	133.6	0.7318	−23.0	98.6	152.2

Regarding first-row results, when compared with the results using DNI and DIF measurements instead of forecasts (Table 3), it is evident that for the analyzed periods, the use of forecasts shows better results for days 0 and 1 regarding MBE. However, there is a deterioration for day 2 and across all forecast horizons regarding the MAE and RMSE.

As for the inner-row test results, when compared with GTI based on DNI and DIF measurements instead of forecasts (Table 4), there is a general deterioration in the results, except for the MBE in unshaded conditions for forecast days 0 and 1. Detailed results for each testing period can be found in Appendix B. The use of the developed transposition model resulted in overall MBE and RMSE values of 33.6 W/m^2 and 169.7 W/m^2, respectively, for the entire forecast horizon. These values show that the model is eneficial for linking irradiance forecast models with energy generation modeling in solar power plants, aiding in the production of power output forecasts. These forecasts are essential for better decision-making by operators of such energy systems due to the variability of resource and energy demand.

To understand how the mean bias error of DNI and DIF forecasts affects the bias of the computed GTI values, Figure 13 was created. This figure shows the difference between the MBE of GTI from the developed model using forecasts and experimental data as input as a function of the MBE of DNI and DIF predictions for the forecast at day 0. Positive values of this difference are represented with blue circles, while negative values are represented with white circles. For better readability, only periods with an MBE difference of less than 100 W/m^2 are represented, which resulted in excluding only period 1.

Since the MBE of the proposed model is typically negative for the tests carried out (Tables 7 and A5), and considering the relationship between the MBE values for the forecasted DNI and DIF components (when one tends to higher positive values, the other tends to more negative values (Tables 6 and A3) as a consequence of the closure equation and knowing that the MBE of the GHI forecasts is lower), the bias of the GTI using prediction values may decrease as shown in Figure 13 due to a favorable combination of forecast and model errors. This is the reason why the MBE for unshaded conditions using forecast values (Table 7) is lower than the bias error for the same conditions using experimental values (Table 4). However, this trend is not observed for the shaded conditions, where the mean bias error is still lower when using ground-based measurements. A more detailed analysis of these aspects is needed in the future, which extends beyond the scope of the present work. Also, due to spatial resolution limitations, the forecasted variables from ECMWF (current operational horizontal resolution: ~9 km) are identical for the first and second rows in this experiment. In future work, this algorithm should be validated for a larger power plant that encompasses multiple grid points of a high-resolution forecast model at a hectometric scale.

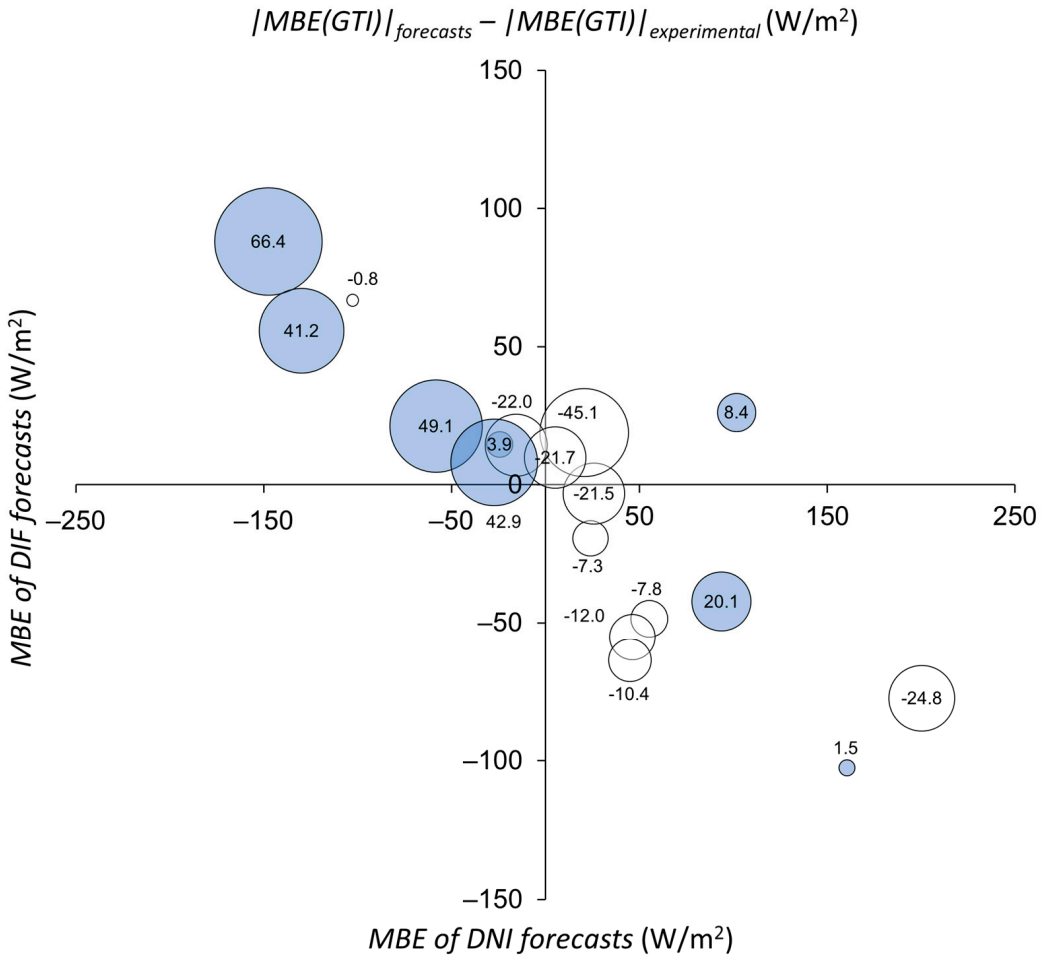

Figure 13. Difference between mean bias errors of GTI from the developed model results using forecasted or experimental data as input for day 0 (negative differences in white and positive differences in blue).

7. Conclusions

This work presented a comprehensive analysis of nine analytical transposition models based on physics alongside the Perez transposition model to compute the global tilted irradiance on photovoltaic module surfaces. Additionally, it presented a model for the computation of this variable in rows of modules other than the first, which usually comprises most rows of solar power plants. The developed model can be applied to any first-row transposition model, provided it considers direct, circumsolar, and isotropic diffuse irradiance. This model computes the GTI for different longitudinal segments of the surfaces of the row of modules, the back of the row in front, and the ground between the rows. It takes into consideration the different view factors and the obscuring of direct and circumsolar irradiance for each of the segments for any apparent solar position and includes the shading effect of the succeeding rows on the ground segments.

The evaluation of these models utilized data collected in Évora, Portugal, for different tilt angles for first-row tests and also for different inter-row distances, including shading conditions, to assess the performance of the developed model. The clearness index helps address potential confounding variables by providing a baseline for sunshine conditions. However, we acknowledge that factors such as wind, relative humidity, precipitation, and aerosols also affect the experiment to some extent. In future research, these factors should be considered. Also, our dataset is limited to our experimental setup. While expanding to diverse locales would enhance generalizability, the focus of this study was on addressing

challenges specific to inner rows of solar panels, rather than aiming for global applicability. Thus, while our findings offer valuable insights, they may not directly apply to all regions.

Results showed that the best analytical transposition model for the first row is the Modified Bugler model, showing an overall MBE of 23.8 W/m^2 and RMSE of 30.5 W/m^2. Conversely, for other rows, the developed model showed an MBE of -12.9 W/m^2 and RMSE of 76.8 W/m^2, resulting in an improvement of 368.3 W/m^2 and 224.4 W/m^2, respectively, compared to using the selected reference transposition model for first rows. This shows the importance of considering the direct shading and obscuring of the sky dome when computing GTI for surfaces in rows that are not the first.

Furthermore, the operational performance of transposition models was evaluated for GTI forecasting, using improved irradiance forecast values instead of measurements of DNI and DIF. These forecast values were obtained from artificial neural network models using numerical weather prediction and aerosol forecast data. Results of the first-row tests showed a MBE and RMSE for all data of 6.7 W/m^2 and 48.7 W/m^2 for forecast day 0, 15.5 W/m^2 and 55.0 W/m^2 for forecast day 1, and 71.5 W/m^2 and 128.5 W/m^2 for forecast day 2. This shows an increased error compared to results using observations which are a mean MBE and RMSE increase across the three days of forecast of 7.4 W/m^2 and 46.9 W/m^2. It also shows how the forecast performance tends to deteriorate with time. The same is visible for the tests performed for other rows, which show an overall MBE and RMSE of -31.5 W/m^2 and 164.0 W/m^2 for forecast day 0, -32.1 W/m^2 and 165.6 W/m^2 for forecast day 1, and -37.2 W/m^2 and 179.4 W/m^2 for forecast day 2.

This work demonstrated that transposition models that neglect shading and irradiance obscuration are not suitable for the accurate estimation of GTI in surfaces that are not in the front row of a solar power plant. The use of a dedicated model for these conditions, such as the one presented in this work, is of great importance, given that GTI is the main factor influencing the energy generation of solar photovoltaic systems.

Author Contributions: Conceptualization, S.P. and P.C.; methodology, S.P. and P.C.; validation, S.P. and P.C.; formal analysis, S.P. and P.C.; investigation, S.P., P.C. and R.S.; data curation, S.P. and P.C.; writing—original draft preparation, S.P.; writing—review and editing, S.P., P.C. and R.S.; visualization, S.P. and P.C.; supervision, P.C. and R.S. All authors have read and agreed to the published version of the manuscript.

Funding: This work was funded by National funds through FCT—Fundação para a Ciência e Tecnologia, I.P. (projects UIDB/04683/2020 and UIDP/04683/2020). S. Pereira acknowledges the support of FCT (the Portuguese Science and Technology Foundation) through the grant with reference SFRH/BD/145378/2019.

Data Availability Statement: The raw data supporting the conclusions of this article will be made available by the authors on request. Restrictions apply to the availability of these data. Data were obtained from ECMWF.

Acknowledgments: The authors are thankful to Afonso Cavaco, Josué Figueira, and Samuel Ramos Bárias for their technical support.

Conflicts of Interest: The authors declare no conflicts of interest.

Glossary

Nomenclature

A	Anisotropy index
BHI	Beam horizontal irradiance (W/m^2)
C	Fraction of circumsolar area obscured by the adjacent row
c	Length along the panel (m)
c_s	Position of the pyranometer along the length of the panel (m)
D	Distance between rows in the horizontal plane (m)
$\vec{D}$	Vector of diffuse horizontal irradiance vector (W/m^2)
D_{cs}	Circumsolar diffuse component of GTI (W/m^2)
DIF	Diffuse horizontal irradiance (W/m^2)
D_{iso}	Isotropic diffuse component of GTI (W/m^2)
DNI	Direct normal irradiance (W/m^2)
EHI	Extraterrestrial horizontal irradiance (W/m^2)
ENI	Extraterrestrial normal irradiance (W/m^2)
F	View factor matrix
F_g	Ground view factor
F_s	Sky view factor
f	Clearness index as defined in the Klucher model
GTI	Global tilted irradiance (W/m^2)
GRI	Global reflected irradiance (W/m^2)
h_0	Vertical distance between the ground and the panel base (m)
I	Identity matrix
I_b	Direct component of GTI (W/m^2)
$\vec{I}_r$	Vector of direct horizontal irradiance vector (W/m^2)
I_{refl}	Reflection component of GTI (W/m^2)
k_T	Clearness index
L	Length of the panel (m)
MAE	Mean absolute error (W/m^2)
MBE	Mean bias error (W/m^2)
MAPE	Mean absolute percentage error (%)
R	Reflectivity matrix
R_b	Beam irradiance tilt factor
R_d	Diffuse irradiance tilt factor
RMSE	Root-mean-squared error (W/m^2)
RMSPE	Root-mean-squared percentage error (%)
R^2	Coefficient of determination
R_r	Reflected irradiance tilt factor
r	Apparent angular radius of circumsolar irradiance (°)
S	Shading of direct component coefficient
S_{cs}	Shading of circumsolar component coefficient
u	Length along the ground (m)
v	Length along the back of the front panel (m)
W	Row width (m)
w_i	Weight of irradiance component i to the bias reduction (%)
X_i	Isotropic component of first-row model
X_{cs}	Circumsolar component of first-row model

Acronyms

ANN	Artificial neural networks
CAMS	Copernicus Atmospheric Monitoring Service
ECMWF	European Centre for Medium-range Weather Forecasts
IFS	Integrated forecasting system
NWP	Numerical weather prediction

Greek symbols

Φ	Solar zenith angle (°)
α	Solar elevation angle (°)
α'	Projection of α in the vertical plane of the local meridian (°)
β	Surface tilt angle (°)
γ_p	Surface azimuth (°)
γ_s	Solar azimuth (°)
δ	Angle between the horizontal and the top of the front panel (°)
ε	Angle between the horizontal and the top of the panel being considered (°)
ζ	Angle between the horizontal and the bottom of the front panel (°)
θ	Angle of incidence (°)
λ	Angle between the horizontal and the bottom of the panel being considered (°)
ξ	Angle between the horizontal and the top of the panel in front of the front panel (°)
ρ	Ground albedo
σ	Angle between the horizontal and the top of the panel behind the panel being considered (°)

Appendix A

The flowchart of the model used to generate forecast data of direct normal irradiance (DNI) [22] used in this work is shown in Figure A1.

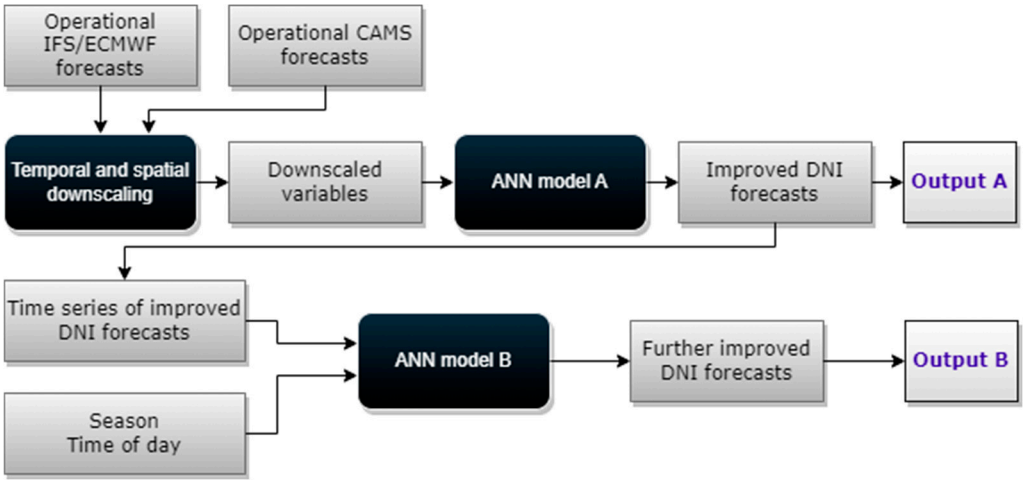

Figure A1. Flowchart of the model used to generate DNI forecasts [22].

The model takes as input data the variables shown in Table A1 from the operational Integrated Forecasting System (IFS) of the European Centre for Medium-range Weather Forecasts (ECMWF) and the Copernicus Atmospheric Monitoring Service (CAMS). These are run every day at 00 UTC, providing hourly forecast values up to 90 h ahead at discrete points of a global grid with a horizontal spatial resolution of 0.125° × 0.125°.

A temporal and spatial downscaling is performed on these variables, which results in forecasts for a specific location and higher temporal resolution. This downscaling is obtained through a bi-linear interpolation of the values in the four surrounding grid points of the desired location for the spatial downscaling and a piecewise cubic hermite interpolation of the hourly values into smaller timesteps (in this work, it was 10 min values) for the temporal downscaling.

Table A1. Input variables obtained from numerical weather prediction models.

Variables Obtained from IFS/ECMWF	Variables Obtained from CAMS
Direct normal irradiance	Total aerosol optical depth at 670 nm
Global horizontal irradiance	Total aerosol optical depth at 865 nm
Low cloud cover	Total aerosol optical depth at 1240 nm
Medium cloud cover	Sea salt aerosol optical depth at 550 nm
High cloud cover	
Total cloud cover	
Wind speed	
Air temperature	
Solar zenith angle	

The downscaled variables are then fed to an artificial neural network (ANN model A), which is a feed-forward network with one hidden layer comprising seven neurons and uses (i) a backpropagation learning function, namely Bayesian regularization backpropagation; (ii) a linear layer output with an initialization function that initializes the weights and biases of the layers according to the Nguyen–Widrow initialization algorithm; (iii) the hyperbolic tangent sigmoid transfer function; and (iv) the mean-squared error as a performance function. The input and output data are processed by removing rows with constant values and scaling the mean of each row to 0 and deviations to 1. This ANN takes into consideration the nonlinear relationships between the different atmospheric and aerosol variables and DNI resulting in improved DNI forecasts for the specified location and temporal resolution.

A second artificial neural network (ANN model B) is similar to ANN model A, but uses the Levenberg–Marquardt backpropagation algorithm and has eight neurons in the hidden layer, taking as input a time series of 12 timesteps of the improved DNI forecasts prior to the forecast moment (from the output of the ANN model A) along with the season and time of day. This model takes into consideration the temporal variation in DNI and further improves the DNI forecasts from ANN model A.

Appendix B

Table A2. Metrics of DNI and DIF forecasts for the measuring periods used for first-row tests (MBE, MAE, and RMSE in W/m^2).

Period and Variable		Day 0				Day 1				Day 2			
		R^2	MBE	MAE	RMSE	R^2	MBE	MAE	RMSE	R^2	MBE	MAE	RMSE
1	DNI	0.5114	−33.1	57.0	87.6	0.6120	−14.9	38.3	67.9	0.4664	−15.3	72.2	99.5
	DIF	0.1228	18.5	26.5	39.1	0.2874	6.0	11.0	13.7	0.0912	−2.8	32.0	37.9
2	DNI	0.9082	−68.7	68.9	72.7	0.7794	−30.4	39.5	58.6	0.6228	−36.1	61.6	85.1
	DIF	0.8119	40.8	41.1	46.5	0.0063	6.8	15.9	21.1	0.0019	7.0	31.7	36.5
3	DNI	0.3542	−50.9	92.0	115.0	0.0803	−17.7	175.5	204.5	0.0014	−13.2	131.0	164.0
	DIF	0.6937	−8.7	59.7	70.4	0.5290	0.6	78.9	86.8	0.6843	−9.4	70.4	77.7
4	DNI	0.2470	47.4	74.0	127.7	0.2273	−33.2	79.1	128.7	0.1022	−322.1	322.1	391.3
	DIF	0.2873	−57.5	58.4	94.0	0.4425	−24.5	40.2	69.2	0.4884	11.7	43.2	69.3
5	DNI	0.4456	−86.6	149.2	220.4	0.1410	−121.6	206.9	283.7	0.2980	−132.1	180.7	256.1
	DIF	0.5380	−3.2	32.5	39.9	0.0513	33.5	57.9	70.8	0.0195	36.9	65.1	76.6

Table A3. DNI and DIF forecast results for the measuring periods used for testing of the developed model (MBE, MAE, and RMSE in W/m^2).

Period and Variable		Day 0				Day 1				Day 2			
		R^2	MBE	MAE	RMSE	R^2	MBE	MAE	RMSE	R^2	MBE	MAE	RMSE
1	DNI	0.1957	26.3	101.8	141.4	0.1127	14.1	92.3	146.1	0.0151	−28.4	128.6	162.6
	DIF	0.1687	−59.2	64.2	76.0	0.4663	−36.4	36.9	52.9	0.0006	4.7	59.5	67.6
2	DNI	0.9552	55.4	55.6	66.8	0.4768	28.5	59.8	80.9	0.9153	9.4	21.7	33.9
	DIF	0.5153	−48.5	48.5	52.3	0.0240	−20.4	31.3	40.1	0.2740	−23.8	30.7	39.8
3	DNI	0.6753	24.0	121.2	190.3	0.6811	−16.6	134.1	187.7	0.6930	2.9	134.2	184.3
	DIF	0.6857	−19.4	48.7	72.4	0.6798	−15.5	51.3	71.1	0.5439	−15.4	60.7	85.3
4	DNI	0.0879	46.2	178.6	273.2	0.1934	59.5	162.1	253.6	0.2277	51.8	162.0	251.3
	DIF	0.2560	−55.3	63.1	97.3	0.5052	−60.9	65.2	90.1	0.4056	−55.6	64.6	91.0
5	DNI	0.1872	−58.2	106.8	140.4	0.0197	−45.0	133.4	184.8	0.0065	0.4	83.2	149.6
	DIF	0.1999	21.2	40.3	46.0	0.0189	−11.8	38.5	58.5	0.0143	−4.1	35.6	56.4
6	DNI	0.3289	−147.5	169.6	210.3	0.3673	46.18	47.2	89.7	0.3013	38.0	46.6	89.3
	DIF	0.0152	88.0	96.9	129.0	0.0550	−33.5	33.5	46.3	0.0019	−25.4	28.5	44.2
7	DNI	0.8260	−24.4	36.7	44.5	0.8981	11.9	31.0	37.3	0.8394	37.6	49.0	65.9
	DIF	0.6205	14.6	22.6	28.4	0.4374	−3.9	23.9	26.6	0.0125	−25.9	38.1	49.2
8	DNI	0.8672	25.8	53.5	60.2	0.8169	30.5	74.9	85.3	0.8656	57.5	61.8	69.2
	DIF	0.5586	−3.2	11.8	15.8	0.3760	−13.7	26.8	30.6	0.0822	−26.5	26.5	30.9
9	DNI	0.1415	160.6	213.8	270.0	0.1635	99.9	184.8	223.0	0.0117	190.2	290.4	341.6
	DIF	0.3964	−102.6	115.7	143.9	0.0298	−96.5	126.6	157.6	0.0196	−102.5	131.1	161.4
10	DNI	0.3396	93.7	196.6	266.0	0.2661	33.3	204.1	268.5	0.4108	−20.3	201.3	235.9
	DIF	0.2564	−42.3	90.2	122.9	0.2894	−20.0	85.2	113.8	0.3719	−17.3	87.1	105.8
11	DNI	0.2717	−129.9	170.9	207.2	0.6058	−42.8	83.0	111.2	0.6257	22.0	69.2	103.2
	DIF	0.0832	55.7	70.8	96.5	0.0929	22.9	37.4	45.3	0.3765	−7.9	23.0	30.9
12	DNI	0.0420	45.0	197.2	228.6	0.1069	95.6	258.8	310.0	0.3188	197.5	295.7	363.3
	DIF	0.5633	−63.8	97.1	113.2	0.6490	−114.3	128.1	152.1	0.7377	−108.5	121.3	150.0
13	DNI	0.2652	200.3	217.9	265.3	0.2650	231.0	252.1	300.2	0.2762	262.2	299.9	341.5
	DIF	0.1240	−77.5	104.1	127.2	0.1153	−99.3	119.9	141.8	0.1656	−119.1	135.3	154.5
14	DNI	0.3747	101.8	137.5	163.5	0.4259	156.6	162.3	210.6	0.2201	107.0	145.8	186.7
	DIF	0.4555	26.2	89.6	111.4	0.4369	14.8	85.0	112.2	0.4314	55.2	95.9	122.8
15	DNI	0.1945	−102.7	125.5	161.5	0.2203	−148.3	173.5	190.0	0.2292	−116.1	139.4	170.9
	DIF	0.3872	66.8	68.7	93.0	0.4400	81.7	81.7	97.4	0.4533	73.0	76.7	102.6
16	DNI	0.0805	20.7	230.0	265.3	0.1606	−34.3	209.9	246.7	0.0197	−197.8	326.9	405.4
	DIF	0.5675	18.9	53.0	65.6	0.4792	31.2	64.2	77.2	0.7111	−15.6	46.0	52.8
17	DNI	0.3496	−15.5	92.7	146.0	0.4274	−37.6	119.2	158.3	0.4238	−96.0	151.4	205.5
	DIF	0.1479	14.3	29.4	38.5	0.2745	11.2	31.1	39.7	0.3782	31.2	41.1	50.6
18	DNI	0.0262	5.2	145.8	211.6	0.0983	19.4	139.8	198.7	0.0154	39.0	142.2	210.7
	DIF	0.0994	9.8	76.4	102.3	0.1921	3.7	72.6	95.8	0.0518	−4.0	81.5	111.6
19	DNI	0.7739	−27.3	65.6	99.7	0.8940	0.1	42.2	67.5	0.7421	−33.4	89.0	121.4
	DIF	0.4384	8.1	20.8	27.4	0.8150	−2.1	12.9	18.2	0.0654	34.8	45.4	60.6

Table A4. GTI metrics of first-row tests for each day of forecast horizon and for each period using the Modified Bugler transposition model with DNI and DIF forecasts (MBE, MAE, and RMSE in W/m^2).

Period	Day 0				Day 1				Day 2			
	R^2	MBE	MAE	RMSE	R^2	MBE	MAE	RMSE	R^2	MBE	MAE	RMSE
1	0.9795	29.2	33.5	46.4	0.9798	29.5	35.6	46.4	0.9719	23.0	41.4	48.7
2	0.9980	8.9	13.8	16.6	0.9941	12.7	22.6	25.6	0.9933	11.0	23.8	27.7
3	0.9224	−29.4	45.4	63.9	0.9511	31.6	45.7	65.9	0.9345	16.3	36.4	56.3
4	0.9177	9.8	44.7	59.4	0.8715	19.8	51.8	74.6	0.0893	−203.9	210.1	277.7
5	0.9633	21.6	34.9	40.6	0.9329	21.8	41.7	48.4	0.9742	47.0	29.9	34.6

Table A5. GTI results of the developed model for rows that are not the front row for each day of forecast horizon and for each period using DNI and DIF forecasts (MAE and RMSE in W/m2, MAPE and RMSPE in %).

Period	Day 0				Day 1				Day 2			
	R^2	MBE	MAE	RMSE	R^2	MBE	MAE	RMSE	R^2	MBE	MAE	RMSE
1	0.0043	−163.0	207.1	364.9	0.0059	−163.5	195.8	364.0	0.0048	−179.4	215.5	365.9
2	0.9913	−30.7	34.9	38.8	0.9835	−41.0	42.7	57.2	0.9768	−50.3	53.2	70.5
3	0.6449	−17.4	117.5	175.0	0.6302	−36.0	129.9	181.5	0.5980	−25.8	128.2	187.2
4	0.3640	−3.7	81.8	137.8	0.3764	−3.0	84.0	138.3	0.3630	1.1	85.3	142.8
5	0.4550	−87.7	108.9	214.5	0.4017	−99.6	131.8	234.1	0.4038	−72.3	105.8	217.9
6	0.9196	−105.8	113.3	141.0	0.9651	−29.2	45.2	57.8	0.9636	−30.8	46.8	59.7
7	0.9938	−43.3	43.8	48.8	0.9981	−31.1	31.6	35.0	0.9971	−26.5	27.0	30.9
8	0.9958	−48.0	50.0	52.5	0.9963	−50.2	51.5	53.8	0.9949	−49.7	51.7	54.6
9	0.1442	−82.6	112.5	166.3	0.1479	−93.7	114.7	166.2	0.0815	−84.5	127.3	179.2
10	0.1607	−62.4	142.8	242.5	0.1907	−78.1	143.9	239.9	0.2246	−105.8	147.0	242.8
11	0.8884	−92.8	97.4	125.5	0.9728	−62.1	67.4	78.0	0.9823	−37.5	44.1	51.3
12	0.5099	−43.6	108.8	150.6	0.4232	−36.7	136.7	181.2	0.5488	44.0	111.4	167.7
13	0.9111	19.9	57.1	71.5	0.9154	28.6	54.7	71.8	0.9025	41.8	64.9	87.6
14	0.1142	95.4	105.1	135.2	0.1097	107.8	113.6	155.5	0.0710	111.3	121.3	155.7
15	0.8651	−61.9	74.8	91.6	0.8613	−68.5	87.4	96.9	0.8723	−64.5	78.0	91.8
16	0.4764	5.2	166.3	204.4	0.4233	−30.8	172.6	212.8	0.0174	−227.0	295.8	380.3
17	0.9180	−43.9	70.8	85.8	0.9211	−59.2	76.7	91.8	0.9147	−79.1	90.5	107.8
18	0.8772	−41.7	81.4	99.7	0.8803	−39.9	78.1	97.9	0.8741	−41.9	83.2	100.8
19	0.6672	−55.3	65.9	114.3	0.6605	−51.8	62.1	114.6	0.6384	−39.4	51.7	109.7

References

1. SolarPower Europe. *Global Market Outlook for Solar Power 2023–2027*; SolarPower Europe: Brussels, Belgium, 2023. Available online: https://www.solarpowereurope.org/insights/market-outlooks/global-market-outlook-for-solar-power-2023-2027-1 (accessed on 5 June 2024).
2. *International Energy Agency Renewables 2023*; Analysis and Forecast to 2028; International Energy Agency: Paris, France, 2023.
3. Nassar, Y.F.; Hafez, A.A.; Alsadi, S.Y. Multi-Factorial Comparison for 24 Distinct Transposition Models for Inclined Surface Solar Irradiance Computation in the State of Palestine: A Case Study. *Front. Energy Res.* **2020**, *7*, 1–19. [CrossRef]
4. Yang, D. Solar Radiation on Inclined Surfaces: Corrections and Benchmarks. *Sol. Energy* **2016**, *136*, 288–302. [CrossRef]
5. Gueymard, C.A. Direct and Indirect Uncertainties in the Prediction of Tilted Irradiance for Solar Engineering Applications. *Sol. Energy* **2009**, *83*, 432–444. [CrossRef]
6. Gueymard, C. An Anisotropic Solar Irradiance Model for Tilted Surfaces and Its Comparison with Selected Engineering Algorithms. *Sol. Energy* **1987**, *38*, 367–386. [CrossRef]
7. Klucher, T.M. Evaluation of Models to Predict Insolation on Tilted Surfaces. *Sol. Energy* **1979**, *23*, 111–114. [CrossRef]
8. Hay, J.E. Calculating Solar Radiation for Inclined Surfaces: Practical Approaches. *Renew. Energy* **1993**, *3*, 373–380. [CrossRef]
9. Hay, J.; McKay, D. *Final Report IEA Task IX-Calculation of Solar Irradiances for Inclined Surfaces: Verification of Models Which Use Hourly and Daily Data*; International Energy Agency: Paris, France, 1988.
10. Nassar, Y.F.; Abuhamoud, N.M.; Miskeen, G.M.; El-Khozondar, H.J.; Alsadi, S.Y.; Ahwidi, O.M. Investigating the Applicability of Horizontal to Tilted Sky-Diffuse Solar Irradiation Transposition Models for Key Libyan Cities. In Proceedings of the 2022 IEEE 2nd International Maghreb Meeting of the Conference on Sciences and Techniques of Automatic Control and Computer Engineering (MI-STA 2022), Sabratha, Libya, 23–25 May 2022; pp. 9–14. [CrossRef]

11. Mayer, M.J.; Gróf, G. Extensive Comparison of Physical Models for Photovoltaic Power Forecasting. *Appl. Energy* **2021**, *283*, 116239. [CrossRef]
12. Khan, M.M.; Ahmad, M.J. Estimation of Global Solar Radiation Using Clear Sky Radiation in Yemen. *J. Eng. Sci. Technol. Rev.* **2012**, *5*, 12–19. [CrossRef]
13. Padovan, A.; Del Col, D. Measurement and Modeling of Solar Irradiance Components on Horizontal and Tilted Planes. *Sol. Energy* **2010**, *84*, 2068–2084. [CrossRef]
14. Muneer, T.; Gueymard, C.; Kambezidis, H. Hourly Slope Irradiation and Illuminance. In *Solar Radiation and Daylight Models*; Butterworth-Heinemann: Oxford, UK, 2004; p. 143. [CrossRef]
15. Badescu, V. 3D Isotropic Approximation for Solar Diffuse Irradiance on Tilted Surfaces. *Renew. Energy* **2002**, *26*, 221–233. [CrossRef]
16. Tian, Y.Q.; Davies-Colley, R.J.; Gong, P.; Thorrold, B.W. Estimating Solar Radiation on Slopes of Arbitrary Aspect. *Agric. Meteorol.* **2001**, *109*, 67–74. [CrossRef]
17. Appelbaum, J.; Massalha, Y.; Aronescu, A. Corrections to Anisotropic Diffuse Radiation Model. *Sol. Energy* **2019**, *193*, 523–528. [CrossRef]
18. Varga, N.; Mayer, M.J. Model-Based Analysis of Shading Losses in Ground-Mounted Photovoltaic Power Plants. *Sol. Energy* **2021**, *216*, 428–438. [CrossRef]
19. Tschopp, D.; Jensen, A.R.; Dragsted, J.; Ohnewein, P.; Furbo, S. Measurement and Modeling of Diffuse Irradiance Masking on Tilted Planes for Solar Engineering Applications. *Sol. Energy* **2022**, *231*, 365–378. [CrossRef]
20. ECMWF IFS Documentation. Available online: https://www.ecmwf.int/en/publications/ifs-documentation (accessed on 10 December 2021).
21. Pereira, S.; Abreu, E.F.M.; Iakunin, M.; Cavaco, A.; Salgado, R.; Canhoto, P. Method for Solar Resource Assessment Using Numerical Weather Prediction and Artificial Neural Network Models Based on Typical Meteorological Data: Application to the South of Portugal. *Sol. Energy* **2022**, *236*, 225–238. [CrossRef]
22. Pereira, S.; Canhoto, P.; Salgado, R. Development and Assessment of Artificial Neural Network Models for Direct Normal Solar Irradiance Forecasting Using Operational Numerical Weather Prediction Data. *Energy AI* **2023**, *15*, 100314. [CrossRef]
23. Liu, B.Y.H.; Jordan, R.C. The Long-Term Average Performance of Flat-Plate Solar-Energy Collectors. *Sol. Energy* **1963**, *7*, 53–74. [CrossRef]
24. Bugler, J.W. The Determination of Hourly Insolation on an Inclined Plane Using a Diffuse Irradiance Model Based on Hourly Measured Global Horizontal Insolation. *Sol. Energy* **1977**, *19*, 477–491. [CrossRef]
25. Temps, R.C.; Coulson, K.L. Solar Radiation Incident upon Slopes of Different Orientations. *Sol. Energy* **1977**, *19*, 179–184. [CrossRef]
26. Iqbal, M. *An Introduction to Solar Radiation*; Elsevier: Vancouver, BC, Canada, 1983. ISBN 9780123737502.
27. Kasten, F. A New Table and Approximation Formula for the Relative Optial Air Mass. *Arch. Für. Meteorol. Geophys. Und. Bioklimatol. Ser. B* **1965**, *14*, 206–223. [CrossRef]
28. Reindl, D.T.; Beckman, W.A.; Duffie, J.A. Evaluation of Hourly Tilted Surface Radiation Models. *Sol. Energy* **1990**, *45*, 9–17. [CrossRef]
29. Perez, R.; Ineichen, P.; Seals, R.; Michalsky, J.; Stewart, R. Modeling Daylight Availability and Irradiance Components from Direct and Global Irradiance. *Sol. Energy* **1990**, *44*, 271–289. [CrossRef]
30. Saint-Drenan, Y.-M.; Barbier, T. Data-Analysis and Modelling of the Effect of Inter-Row Shading on the Power Production of Photovoltaic Plants. *Sol. Energy* **2019**, *184*, 127–147. [CrossRef]
31. Maor, T.; Appelbaum, J. View Factors of Photovoltaic Collector Systems. *Sol. Energy* **2012**, *86*, 1701–1708. [CrossRef]
32. Eckert, E.R.G. Radiative Transfer, H. C. Hottel and A. F. Sarofim, McGraw-Hill Book Company, New York, 1967. 52 Pages. *AIChE J.* **1969**, *15*, 794–796. [CrossRef]
33. ASD FieldSpec® HandHeld 2 User Manual 2010, 1–140. Available online: https://www.geo-informatie.nl/courses/grs60312/material2017/manuals/600860-dHH2Manual.pdf (accessed on 5 June 2024).
34. Cavaco, A.; Canhoto, P.; Collares Pereira, M. Procedures for Solar Radiation Data Gathering and Processing and Their Application to DNI Assessment in Southern Portugal. *Renew. Energy* **2021**, *163*, 2208–2219. [CrossRef]
35. Long, C.N.; Dutton, E.G. BSRN Global Network Recommended QC Tests, V2.0. Available online: https://epic.awi.de/id/eprint/30083/1/BSRN_recommended_QC_tests_V2.pdf (accessed on 28 May 2024).
36. *ISO 9847:1992*; Solar Energy—Calibration of Field Pyranometers by Comparison to a Reference Pyranometer. International Standard Organization: Geneva, Switzerland, 1992.
37. Betti, A.; Blanc, P.; David, M.; Saint-Drenan, Y.-M.; Driesse, A.; Freeman, J.; Fritz, R.; Gueymard, C.; Habte, A.; Höller, R.; et al. *Best Practices Handbook for the Collection and Use of Solar Resource Data for Solar Energy Applications, Report IEA-PVPS 16-04:2021*, 3rd ed.; International Energy Agency: Paris, France, 2021; ISBN 978-3-907281-19-2.